RESEARCH ARTICLE



WILEY

Thermal insulation versus capacitance: A simulation experiment comparing effects of shade and hyporheic exchange on daily and seasonal stream temperature cycles

S. Kathleen Fogg¹ | Ann Marie Reinhold^{1,2,3} | Scott J. O'Daniel⁴ | Amanda A. Hyman¹ | Geoffrey C. Poole^{1,3} |

Correspondence

S. Kathleen Fogg, Department of Land Resources and Environmental Sciences, Montana State University, Bozeman, MT, USA. Email: sarah.fogg@montana.edu

Present address

Amanda A. Hyman, Department of Biological Sciences, Virginia Polytechnic Institute and State University, Blacksburg, Virginia, USA.

Funding information

National Science Foundation EPSCoR, Grant/Award Number: OIA-1757351; US DOE Bonneville Power Administration, Grant/Award Number: 2007-252-00; USDA National Institute of Food and Agriculture, Grant/Award Number: 1015745

Abstract

In streams where water temperatures stress native biota, management of riparian shade or hyporheic exchange are both considered viable management strategies for reducing the peaks of daily and seasonal stream channel temperature cycles. Although shade and hyporheic exchange may have similar effects on stream temperatures, their mechanisms differ. Improved understanding of the heat-exchange mechanisms influenced by shade and hyporheic exchange will aid in the appropriate application of either stream temperature management strategy. To illustrate a conceptual model highlighting shade as 'thermal insulation' and hyporheic exchange imparting 'thermal capacitance' to a stream reach, we conducted an in-silico simulation modelling experiment increasing shade or hyporheic exchange parameters on an idealized, hypothetical stream. We assessed the potential effects of increasing shade or hyporheic exchange on a stream reach using an established process-based heat-energy budget model of stream-atmosphere heat exchange and incorporated an advection-driven hyporheic heat exchange routine. The model tracked heat transport through the hyporheic zone and exchange with the stream channel, while including the effects of hyporheic water age distribution on upwelling hyporheic temperatures. Results showed that shade and hyporheic exchange similarly damped diurnal temperature cycles and differentially altered seasonal cycles of our theoretical stream. In winter, hyporheic exchange warmed simulated channel temperatures whereas shade had little effect. In summer, both shade and hyporheic exchange cooled channel temperatures, though the effects of shade were more pronounced. Our simple-to-grasp analogies of 'thermal insulation' for shade effects and 'thermal capacitance' for hyporheic exchange effects on stream temperature encourage more accurate conceptualization of complex, dynamic heat exchange processes among the atmosphere, stream channel, and alluvial aguifer.

KEYWORDS

computer simulation, floodplain, heat budget, hyporheic exchange, restoration, riparian, shade, stream temperature

This is an open access article under the terms of the Creative Commons Attribution-NonCommercial-NoDerivs License, which permits use and distribution in any medium, provided the original work is properly cited, the use is non-commercial and no modifications or adaptations are made.

© 2023 The Authors. *Hydrological Processes* published by John Wiley & Sons Ltd.

¹Department of Land Resources and Environmental Sciences, Montana State University, Bozeman, Montana, USA

²Gianforte School of Computing, Montana State University, Bozeman, Montana, USA

³Montana Institute on Ecosystems, Montana State University, Bozeman, Montana, USA

⁴Confederated Tribes of the Umatilla Indian Reservation, Pendleton, Oregon, USA



1 | INTRODUCTION

Stream channel temperature is a common management focus as temperature is a first-order control on many in-stream ecosystem processes. For instance, channel temperature influences nutrient cycling, respiration rates (Jankowski et al., 2014; Manning et al., 2018), oxygen availability (Harvey et al., 2011), growth rates of in-stream plant and animal species (Ficke et al., 2007; Mottola et al., 2020; Till et al., 2019), and the overall community structure of a stream reach (Haase et al., 2019). The detrimental effects of warming stream temperatures is often a primary management concern and the effects on stream ecology to warming stream temperatures is well documented in the literature (i.e., Demars et al., 2011; Hester & Doyle, 2011; Mote et al., 2003; Pound et al., 2021).

In the inter-mountain western U.S., declining populations of native, cold-water salmonids has led to management practices designed to promote the health and survival of these populations. Particular focus has been on management of stream channel thermal regimes as salmonid species are sensitive to thermal stressors (Richter & Kolmes, 2005). Additionally, salmonids rely on expansive, coarse-grained floodplain stream reaches with high hyporheic exchange as they provide essential spawning gravels and habitats across all life-stages (Hauer et al., 2016). Because of the importance of coarse-grained floodplain reaches to native salmonids, management of the thermal regimes of these reaches is of particular interest.

Common practices for managing stream temperatures leverage the natural heat exchange processes of a stream—specifically, riparian vegetative shade or hyporheic exchange (Hester & Gooseff, 2010; Kurylyk et al., 2015). Both shade and hyporheic exchange have been shown to reduce the daily means and amplitudes of temperature cycles in the summer months (Arrigoni et al., 2008; Moore et al., 2005; Poole & Berman, 2001). In the western U.S., riparian improvements are overwhelmingly more common and less costly than channel reconfigurations to increase hyporheic exchange (Follstad Shah et al., 2007; Katz et al., 2007).

Understanding the potential effects of a restoration action a priori will likely lead to improved management decisions. Studies utilizing mechanistic modelling experiments to inform stream restoration and management guidelines are becoming more common in the literature (see Bobst et al., 2022; Chu et al., 2013; DeWalle, 2008; Justice et al., 2017). Conceptual models of common temperature-restoration practices, such as shade and hyporheic exchange improvements, would provide useful generalizations of heat exchange processes and may increase mechanistic understanding of the effects of increasing shade or hyporheic exchange on stream channel heat budgets.

We propose mechanistic conceptual models of shade and hyporheic exchange, where shade imparts 'thermal insulation' to a stream channel and hyporheic exchange affects the 'thermal capacitance'. Channel shade from riparian vegetation acts as an 'insulator' by affecting heat exchange mechanisms across the stream channel-atmosphere interface. Shade reduces the solar radiative load on the channel (Beschta, 1997; O'Briain et al., 2020) and increases in vegetation increase downward longwave radiation. In contrast, hyporheic

exchange influences the heat capacitance of the streambed. Water and associated heat from downwelling stream water is stored in the hyporheic zone before being released after a time-lag, thus acting as a 'capacitor' of heat. Mixing of upwelling hyporheic water and channel water alters the temperature of the stream channel.

We demonstrate these conceptual models of shade and hyporheic exchange by conducting an in silico simulation modelling experiment where we systematically varied shade and hyporheic exchange using a river heat-energy budget model. Advection of heat is the dominant process of hyporheic exchange in floodplain reaches with coarse-grained alluvium. Conventional heat-energy budget models consider conductive heat exchange with the streambed (Dugdale et al., 2017; Ouellet et al., 2014; but see Marzadri et al., 2013), but do not simulate the bidirectional exchange of water and associated advective heat exchange between the channel and hyporheic zone (e.g., Abdi & Endreny, 2019; Boyd & Kasper, 2003; Glose et al., 2017, and others). Instead, increasing the thermal conductivity associated with a channel-streambed conduction equation provides a coarse mechanism for representing thermal effects of systems with high hyporheic exchange (Webb & Zhang, 1997). In our heat-energy model we use a novel representation of hyporheic heat exchange based on methods presented by Poole et al. (2022), which simulates advection by storing and releasing water and associated heat from the hyporheic zone based on a power-law exit-age distribution (also known as 'residence time distribution'). This method allows us to simulate the dynamic and interdependent nature of channel and hyporheic temperatures (Faulkner et al., 2020; Munz et al., 2017), and to accurately represent the effects of high gross hyporheic exchange rates on channel temperatures.

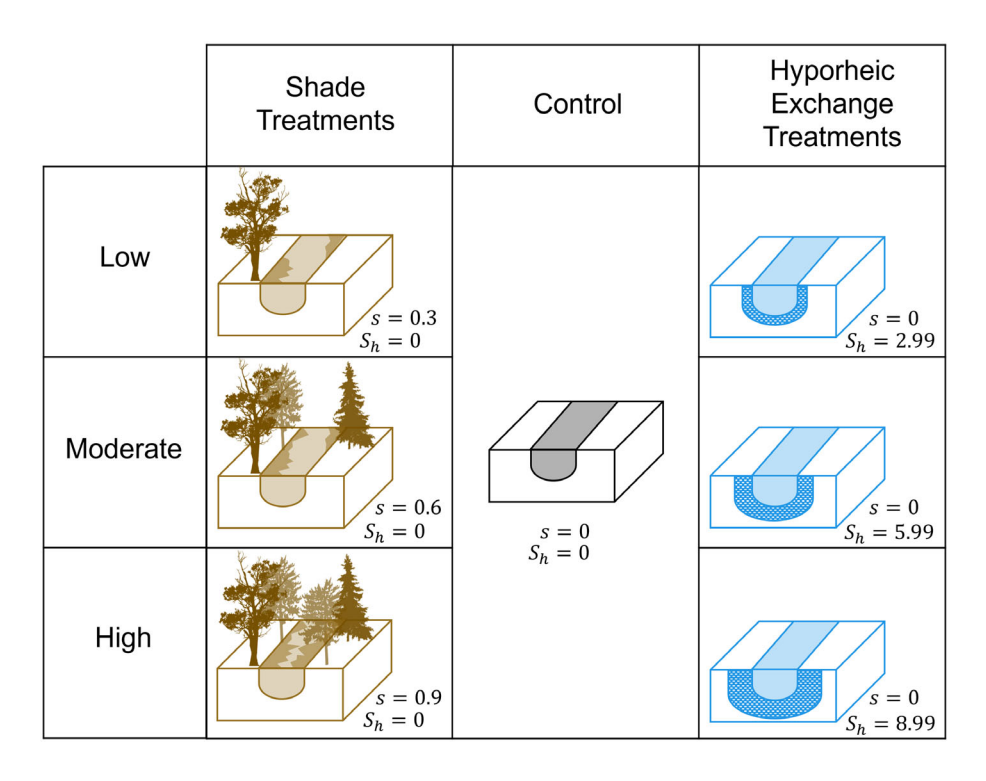
Our objectives were to (1) simulate channel temperature and heat budget changes that may result from restoration of shade or hyporheic exchange, (2) accurately represent the effects of hyporheic heat exchange on channel temperatures of floodplain reaches by modelling advection in the hyporheic zone, and (3) present mechanistic conceptual models to summarize the effects of shade and hyporheic restorations on channel temperatures. We present a simple modelling experiment to demonstrate the potential effects of increasing shade or increasing hyporheic exchange on a stream reach's heat budget and temperature cycles at the daily and seasonal scale. In our model, we used generalized parameters and idealized driving variables that would be typical of streams located in the intermountain western U.S., and not of any particular stream reach. This allowed us to present generalizable mechanistic conceptual models of shade as a 'thermal insulator' and hyporheic exchange affecting 'thermal capacitance' to simplify the complex effects that each have on a stream's heat budget.

2 | METHODS

2.1 | Study design

To compare the effects of shade and hyporheic exchange on stream channel temperature, we conducted a simulation experiment where

FIGURE 1 Schematic of experimental design. We simulated three shade treatment scenarios where we incremented the proportion of shade on the channel, *s*, and three hyporheic exchange (HE) treatment scenarios of where we increased the effective hyporheic zone thickness (m). The control scenario had neither shade nor streambed heat exchange.



we systematically varied shade density and hyporheic exchange rates within a physically-based stream temperature model while holding other parameters and driving variables constant (Figure 1). The stream temperature model, 'TempTool', combined well-established equations that represent heat exchange between channel water and the atmosphere (Evans et al., 1998; Webb & Zhang, 1997) with a novel approach to simulating advective heat transport through the hyporheic zone by incorporating estimates of gross bidirectional hyporheic exchange and associated hyporheic exit-age distributions (Poole et al., 2022) using foundational equations from chemical engineering research (Butt, 1999; Coker, 2001; Danckwerts, 1953).

We employed TempTool using a Lagrangian reference by simulating the temperature dynamics of a parcel of stream water as it flowed along a spatially uniform stream with temporally dynamic atmospheric driving variables. The model parameters held constant during our simulation experiments were chosen to be generally representative of a stream similar to the Umatilla River, Oregon, USA, where hyporheic exchange has been shown to influence stream channel temperature (Arrigoni et al., 2008) and for which necessary model parameters have been established by past research (Jones et al., 2008; Poole et al., 2008). Our aim was not to represent temperature dynamics of the Umatilla River exactly, just to represent a stream system akin to it.

As our aim was to demonstrate conceptual models of the effects of shade and hyporheic exchange on stream temperature and heat budgets, our application of the model was intentionally theoretical and heuristic. Although we used the Umatilla River as a representative stream system for model parameters, these parameters were not tuned to field data from the Umatilla River, thus we did not attempt to validate modelled stream or hyporheic temperatures to observed temperatures nor did we attempt to interpret the magnitude of

simulated water temperatures to variations in shade or hyporheic exchange.

Rather, we conducted a broad analysis of overall patterns in model results and related those patterns to various components of the simulated heat budgets, thus revealing nuanced conceptual models about expected stream temperature responses to different levels of shade versus different levels of hyporheic exchange in streams with expansive alluvium and active hyporheic zones.

2.2 | Model development

TempTool is a one-dimensional (vertical) heat exchange model that calculates the net vertical heat flux for channel water (Q_c , kJ s⁻¹ m⁻²) as the sum of shortwave solar radiation (Q_s), longwave radiation (Q_l), latent heat (Q_e), sensible heat (Q_h) and streambed (Q_h) heat fluxes:

$$Q_c = Q_s + Q_l + Q_e + Q_h + Q_b. (1)$$

Positive values of Q_c indicated net heat gain (warming) while negative values indicated net heat loss (cooling) of the channel water (Figure 2).

TempTool's calculations of stream-atmosphere heat exchange $(Q_s, Q_l, Q_e, \text{ and } Q_h)$ were adopted from previous stream temperature models (Evans et al., 1998; Webb & Zhang, 1997) and, therefore, detailed descriptions are presented in Appendix A. Briefly, we followed the approach of Webb and Zhang (1997), using the Bowen ratio to estimate sensible heat flux, Q_h , and a Dalton-like (mass-transfer) evaporation rate equation for our calculation of latent heat flux, Q_e . Rather than use equations from Webb and Zhang (1997) requiring

FIGURE 2 Comparison of traditional stream heat exchange model (a) and TempTool (b). The channel-atmosphere heat exchange equations are identical between models (a and b), and include shortwave radiation (Q_s) , longwave radiation (Q_l) , latent (Q_e) , and sensible heat exchange (Q_h) . Heat exchange across the streambed is represented differently. In (a), heat exchange between the channel and hyporheic zone (Q_b) is represented by an effective conduction equation. In (b), heat exchange with the hyporheic zone is represented by advection of heat into $(Q_{\downarrow l})$, through, and out of $(Q_{\uparrow l})$ and $(Q_{\downarrow l})$ multiple transient storage zones (Q_{l}) within the hyporheic zone. White boxes represent zones of transient heat storage (H_x) and grey arrows represent heat fluxes (Q_x) . Size of storage zones and flux arrows are arbitrary in this graphic and are not representative of any real or simulated storage volume or flux.

net radiation measurements from stream sites, we used solar-path geometry and an atmospheric attenuation model (Campbell & Norman, 1989) to calculate the shortwave radiation flux, Q_s , at the top of the riparian vegetation canopy. Shortwave radiation was then attenuated by riparian vegetation and reflection from the stream surface (Section 2.2.1) to determine the final value of Q_s . To calculate the longwave portion of the radiation budget, Q_l , we used the Stefan-Boltzman Law, which describes radiation emitted from a black-body based on temperature (Evans et al., 1998). We verified these channel-atmosphere equations against a simple water temperature experiment conducted in an insulated mesocosm with an open surface (Appendix B), which resulted in the adjustment of evaporation rate parameters to represent the inter-mountain western U.S. climate.

2.2.1 | Representation of riparian shade

Several of our model scenarios were based on varying the level of stream shading in TempTool. The effects of riparian shade (s, dimensionless fraction) were simulated by reducing the amount of shortwave radiation reaching the channel. Q_s was calculated using:

$$Q_s = (1 - s)(1 - R_s)Q_{s_q}, (2)$$

where, Q_{s_g} is the shortwave radiation flux at the top of the canopy (Appendix A.1, Equation A.1), and R_s is the fraction of shortwave radiation reflected by the water surface (dimensionless).

In the model, riparian shade also altered above-channel emmissivity, affecting the net longwave heat flux (Appendix A.2). Emmisivity above the stream channel, ϵ_s , was calculated as the shade-weighted average of clear-sky atmospheric emmisivity (ϵ_a , see Appendix A.2, Equation A.14) and riparian canopy emmisivity (ϵ_r , see Table 1),

$$\epsilon_s = (1-s)\epsilon_a + s\epsilon_r.$$
 (3)

2.2.2 | Hyporheic water exchange model

Other model scenarios in our experiment varied the rate of hyporheic exchange and associated size of the hyporheic zone. We designed TempTool to simulate advection of heat through the hyporheic zone based on the conceptual model of hyporheic exchange presented in Poole et al. (2022). We envisioned the hyporheic zone as n transient storage zones (TSZs), $z_1...z_n$. Each z_i was defined abstractly as the hyporheic water volume associated with a discrete range of hyporheic water ages $\tau_{i-1} < \tau \le \tau_i$ (Figure 2b), where water age (τ) was defined as the elapsed time since water entered the hyporheic zone. τ_i denotes the maximum water age associated with z_i and τ_0 denotes the minimum age of hyporheic water.

Importantly, because each TSZ was defined as the water volume associated with a specific range of hyporheic water ages, boundaries between TSZs were *not* spatial (Poole et al., 2022). In fact, TempTool tracked only the dynamic water temperature of hyporheic water volumes defined by TSZs.

and-conditions) on Wiley Online Library for rules of use; OA articles are governed by the applicable Creative Commons License

WILEY 5 of 21

TABLE 1 Model parameters.

R_s Shortwave radiation reflected by water surface 0.1 - Webb and Zhang (1997) S_{po} Solar constant 1.367 $kJ s^{-1} m^{-2}$ Iqbal (1983) p_q Atmospheric pressure 845 mbar Observed annual mean, Pendleton, OR (2003) ϕ Latitude 45.67 ° Observed, Pendleton, OR LC Longitude correction 0.08 ° Observed, Pendleton, OR (2003) U Wind speed 0.01 m s ⁻¹ Observed annual mean, Pendleton, OR (2003) a_w Wind function intercept 3.445 × 10 ⁻⁹ m s ⁻¹ Observed annual mean, Pendleton, OR (2003) a_w Wind function intercept 3.445 × 10 ⁻⁹ m s ⁻¹ Observed annual mean, Pendleton, OR (2003) a_w Wind function intercept 3.445 × 10 ⁻⁹ m s ⁻¹ Observed annual mean, Pendleton, OR (2003) a_w Wind function intercept 3.445 × 10 ⁻⁹ m s ⁻¹ Observed, see Appendix C a_w Wind function intercept 3.445 × 10 ⁻⁹ m s ⁻¹ Observed, see Appendix C a_w Wind function slope 1.383 × 10 ⁻⁸ mbar ⁻¹ Observed, see Appendix C a_w Enissivity of riparian canopy		. 2 Model parameters.			
S_{po} Solar constant1.367kJ s^-1 m^-2Iqbal (1983) p_a Atmospheric pressure845mbarObserved annual mean, Pendleton, OR (2003) ϕ Latitude45.67°Observed, Pendleton, OR LC Longitude correction0.08°Observed, Pendleton, OR U Wind speed0.01m s^-1Observed annual mean, Pendleton, OR (2003) a_w Wind function intercept3.445 × 10^-9m s^-1Observed, see Appendix C b_w Wind function slope1.383 × 10^-8mbar^-1Observed, see Appendix C R_i Longwave radiation reflected by water surface0.03-Anderson (1954) c Clear sky deviation factor1.10-Brutsaert and Jirka (1984) e_r Emissivity of riparian canopy0.97-Sobrino et al. (2005) e_w Emissivity of water0.95-Dingman (2015) c_w Specific heat of water at 10°C4192kJ kg^-1 K^-1Kell (1972) r_0 Minimum and maximum water ages considered as hyporheic water60, see Poole et al. (2008)see Poole et al. (2008) r_0 Exponent of power-law hyporheic exit-age distribution1.39-Poole et al. (2008) r_0 Volumetric porosity of hyporheic zone0.25m³ m^-3Sand and gravel, mixed (Fetter, 1994) r_0 Specific heat of hyporheic sediments870kJ kg^-1 K^-1Waples and Waples (2004)		Parameter	Value	Units	Source
Atmospheric pressure 845 mbar Observed annual mean, Pendleton, OR (2003) ϕ Latitude 45.67 ° Observed, Pendleton, OR LC Longitude correction 0.08 ° Observed, Pendleton, OR U Wind speed 0.01 m s ⁻¹ Observed annual mean, Pendleton, OR (2003) σ_w Wind function intercept 3.445 × 10 ⁻⁹ m s ⁻¹ Observed, see Appendix C σ_w Wind function slope 1.383 × 10 ⁻⁸ mbar ⁻¹ Observed, see Appendix C σ_w Wind function slope 1.383 × 10 ⁻⁸ mbar ⁻¹ Observed, see Appendix C σ_w Longwave radiation reflected by water surface σ_w Clear sky deviation factor 1.10 - Brutsaert and Jirka (1984) σ_w Emissivity of riparian canopy 0.97 - Sobrino et al. (2005) σ_w Emissivity of water 0.95 - Dingman (2015) σ_w Specific heat of water at 10°C 4192 kJ kg ⁻¹ K ⁻¹ Kell (1972) σ_w Density of water at 10°C 999.7 kg m ⁻³ Kell (1972) σ_w Minimum and maximum water ages considered as hyporheic water σ_w Exponent of power-law hyporheic exit-age distribution 1.39 - Poole et al. (2008) σ_w Specific heat of hyporheic zone σ_w Specific heat of hyporheic sediments 870 kJ kg ⁻¹ K ⁻¹ Waples and Waples (2004)	R_s	Shortwave radiation reflected by water surface	0.1	-	Webb and Zhang (1997)
$φ$ Latitude 45.67 ° Observed, Pendleton, OR LC Longitude correction 0.08 ° Observed, Pendleton, OR U Wind speed 0.01 m s ⁻¹ Observed, Pendleton, OR U Wind speed 0.01 m s ⁻¹ Observed annual mean, Pendleton, OR q_w Wind function intercept 3.445 × 10 ⁻⁹ m s ⁻¹ Observed, see Appendix C p_w Wind function slope 1.383 × 10 ⁻⁸ mbar ⁻¹ Observed, see Appendix C p_w U Clear sky deviation reflected by water surface 0.03 - Anderson (1954) p_w C Clear sky deviation factor 1.10 - Brutsaert and Jirka (1984) p_w Emissivity of riparian canopy 0.97 - Sobrino et al. (2005) p_w Emissivity of water 0.95 - Dingman (2015) p_w Density of water at 10°C 4192 kJ kg ⁻¹ K ⁻¹ Kell (1972) p_w Density of water at 10°C 999.7 kg m ⁻³ Kell (1972) p_w Density of water at 10°C 999.7 kg m ⁻³ Sobre et al. (2008) p_w Exponent of power-law hyporheic exit-age distribution 1.39 - Poole et al. (2008) p_w Volumetric porosity of hyporheic sediments 870 kJ kg ⁻¹ K ⁻¹ Waples and Waples (2004)	S_{po}	Solar constant	1.367	$\rm kJ~s^{-1}~m^{-2}$	Iqbal (1983)
LC Longitude correction 0.08 ° Observed, Pendleton, OR U Wind speed 0.01 $m s^{-1}$ Observed annual mean, Pendleton, OR (2003) a_w Wind function intercept 3.445 × 10 ⁻⁹ $m s^{-1}$ Observed, see Appendix C b_w Wind function slope 1.383 × 10 ⁻⁸ $mbar^{-1}$ Observed, see Appendix C Observed, see Appendix C Anderson (1954) c Clear sky deviation factor 1.10 - Brutsaert and Jirka (1984) c Emissivity of riparian canopy 0.97 - Sobrino et al. (2005) c Emissivity of water 0.95 - Dingman (2015) c Specific heat of water at 10°C 4192 c KJ kg ⁻¹ K ⁻¹ Kell (1972) c Foole et al. (2008) c Minimum and maximum water ages considered as hyporheic water 1.57 × 107 c Poole et al. (2008) c Exponent of power-law hyporheic exit-age distribution 1.39 - Poole et al. (2008) c Specific heat of hyporheic sediments 870 c Specific heat of hyporheic sediments	p _a	Atmospheric pressure	845	mbar	·
Wind speed 0.01 $m s^{-1}$ Observed annual mean, Pendleton, OR (2003) a_w Wind function intercept 3.445×10^{-9} $m s^{-1}$ Observed, see Appendix C b_w Wind function slope 1.383×10^{-8} $mbar^{-1}$ Observed, see Appendix C k_{I} Longwave radiation reflected by water surface 0.03 - Anderson (1954) k_{I} C Clear sky deviation factor 0.97 - Brutsaert and Jirka (1984) k_{I} Emissivity of riparian canopy 0.97 - Sobrino et al. (2005) k_{I} Emissivity of water 0.95 - Dingman (2015) k_{I} kg $^{-1}$ K- Kell (1972) k_{I} kg $^{-1}$ K- Kell (1972) k_{I} kg $^{-1}$ K- Kell (1972) k_{I} Minimum and maximum water ages considered as hyporheic water k_{I} Exponent of power-law hyporheic exit-age distribution k_{I} Specific heat of hyporheic sediments k_{I} Specific hyporheic hyporhe	ϕ	Latitude	45.67	0	Observed, Pendleton, OR
a_w Wind function intercept 3.445×10^{-9} m s $^{-1}$ Observed, see Appendix C b_w Wind function slope 1.383×10^{-8} mbar $^{-1}$ Observed, see Appendix C R_I Longwave radiation reflected by water surface 0.03 $-$ Anderson (1954) c Clear sky deviation factor 1.10 $-$ Brutsaert and Jirka (1984) ε_r Emissivity of riparian canopy 0.97 $-$ Sobrino et al. (2005) ε_w Emissivity of water 0.95 $-$ Dingman (2015) c_w Specific heat of water at 10° C 4192 kJ kg $^{-1}$ K $^{-1}$ Kell (1972) ρ_w Density of water at 10° C 999.7 kg m $^{-3}$ Kell (1972) τ_0 Minimum and maximum water ages considered as hyporheic water 60 , 1.57×10^{7} sPoole et al. (2008) α Exponent of power-law hyporheic exit-age distribution 1.39 $-$ Poole et al. (2008) Φ Volumetric porosity of hyporheic zone 0.25 m^3 m $^{-3}$ Sand and gravel, mixed (Fetter, 1994) c_s Specific heat of hyporheic sediments 870 kJ kg $^{-1}$ K $^{-1}$ Waples and Waples (2004)	LC	Longitude correction	0.08	0	Observed, Pendleton, OR
b_w Wind function slope 1.383×10^{-8} mbar $^{-1}$ Observed, see Appendix C R_l Longwave radiation reflected by water surface 0.03 $^{-}$ Anderson (1954) c Clear sky deviation factor 1.10 $^{-}$ Brutsaert and Jirka (1984) ε_r Emissivity of riparian canopy 0.97 $^{-}$ Sobrino et al. (2005) ε_w Emissivity of water 0.95 $^{-}$ Dingman (2015) c_w Specific heat of water at 10° C 4192 $_{\rm J}$ kg $^{-1}$ K $^{-1}$ Kell (1972) ρ_w Density of water at 10° C 999.7 kg m $^{-3}$ Kell (1972) τ_0 Minimum and maximum water ages considered as hyporheic water 60 sPoole et al. (2008) τ_0 Water 1.57×10^7 τ_0 Poole et al. (2008) σ Exponent of power-law hyporheic exit-age distribution 1.39 $-$ Poole et al. (2008) σ Volumetric porosity of hyporheic zone 0.25 m^3 m $^{-3}$ Sand and gravel, mixed (Fetter, 1994) σ Specific heat of hyporheic sediments 870 σ σ Waples and Waples (2004)	U	Wind speed	0.01	${\rm m}~{\rm s}^{-1}$	
R _I Longwave radiation reflected by water surface 0.03 - Anderson (1954) c Clear sky deviation factor 1.10 - Brutsaert and Jirka (1984) $\varepsilon_{\rm r}$ Emissivity of riparian canopy 0.97 - Sobrino et al. (2005) $\varepsilon_{\rm w}$ Emissivity of water 0.95 - Dingman (2015) $c_{\rm w}$ Specific heat of water at 10°C 4192 kJ kg ⁻¹ K ⁻¹ Kell (1972) $\rho_{\rm w}$ Density of water at 10°C 999.7 kg m ⁻³ Kell (1972) $\tau_{\rm 0}$, Minimum and maximum water ages considered as hyporheic water 1.57 × 10 ⁷ α Exponent of power-law hyporheic exit-age distribution 1.39 - Poole et al. (2008) $\sigma_{\rm s}$ Specific heat of hyporheic zone 0.25 m ³ m ⁻³ Sand and gravel, mixed (Fetter, 1994) $\sigma_{\rm s}$ Specific heat of hyporheic sediments 870 kJ kg ⁻¹ K ⁻¹ Waples and Waples (2004)	$a_{\rm w}$	Wind function intercept	3.445×10^{-9}	$m\ s^{-1}$	Observed, see Appendix C
Clear sky deviation factor 1.10 - Brutsaert and Jirka (1984) ϵ_r Emissivity of riparian canopy 0.97 - Sobrino et al. (2005) ϵ_w Emissivity of water 0.95 - Dingman (2015) ϵ_w Specific heat of water at 10°C 4192 ϵ_v Ly kg ⁻¹ K ⁻¹ Kell (1972) ϵ_v Density of water at 10°C 999.7 ϵ_v Minimum and maximum water ages considered as hyporheic water ϵ_v water 1.57 × 10 ⁷ ϵ_v Exponent of power-law hyporheic exit-age distribution 1.39 - Poole et al. (2008) ϵ_v Volumetric porosity of hyporheic zone 0.25 ϵ_v Specific heat of hyporheic sediments 870 ϵ_v Waples and Waples (2004)	b_w	Wind function slope	1.383×10^{-8}	${\rm mbar}^{-1}$	Observed, see Appendix C
ε_r Emissivity of riparian canopy0.97-Sobrino et al. (2005) ε_w Emissivity of water0.95-Dingman (2015) c_w Specific heat of water at 10° C4192 $kJ kg^{-1} K^{-1}$ Kell (1972) ρ_w Density of water at 10° C999.7 $kg m^{-3}$ Kell (1972) τ_0 Minimum and maximum water ages considered as hyporheic water60, solid properties and solid properties are solid properties and solid properties are solid properties at a solid properties and solid properties are solid properties at a solid properties at	R_{l}	Longwave radiation reflected by water surface	0.03	-	Anderson (1954)
Emissivity of water 0.95 - Dingman (2015) c_w Specific heat of water at 10° C 4192 kJ kg $^{-1}$ K $^{-1}$ Kell (1972) ρ_w Density of water at 10° C 999.7 kg m $^{-3}$ Kell (1972) τ_0 , Minimum and maximum water ages considered as hyporheic water 1.57×10^7 s Poole et al. (2008) α Exponent of power-law hyporheic exit-age distribution 1.39 - Poole et al. (2008) Φ Volumetric porosity of hyporheic zone 0.25 m 3 m $^{-3}$ Sand and gravel, mixed (Fetter, 1994) c_s Specific heat of hyporheic sediments 870 kJ kg $^{-1}$ K $^{-1}$ Waples and Waples (2004)	С	Clear sky deviation factor	1.10	-	Brutsaert and Jirka (1984)
$c_{\rm w}$ Specific heat of water at 10°C 4192 $_{\rm kJ~kg^{-1}~K^{-1}}$ Kell (1972) $\rho_{\rm w}$ Density of water at 10°C 999.7 $_{\rm kg~m^{-3}}$ Kell (1972) $\tau_{\rm 0}$, Minimum and maximum water ages considered as hyporheic water 1.57 × 10 ⁷ $_{\rm max}$ Poole et al. (2008) $\sigma_{\rm 0}$ Exponent of power-law hyporheic exit-age distribution 1.39 - Poole et al. (2008) $\sigma_{\rm 0}$ Volumetric porosity of hyporheic zone 0.25 $_{\rm m^3~m^{-3}}$ Sand and gravel, mixed (Fetter, 1994) $\sigma_{\rm 0}$ Specific heat of hyporheic sediments 870 $_{\rm kJ~kg^{-1}~K^{-1}}$ Waples and Waples (2004)	ε_r	Emissivity of riparian canopy	0.97	-	Sobrino et al. (2005)
$ρ_w$ Density of water at 10°C999.7kg m $^{-3}$ Kell (1972) $τ_0$, $τ_n$ Minimum and maximum water ages considered as hyporheic water60, 1.57 × 10 7 sPoole et al. (2008) $α$ Exponent of power-law hyporheic exit-age distribution1.39-Poole et al. (2008) $Φ$ Volumetric porosity of hyporheic zone0.25 m^3 m^{-3} Sand and gravel, mixed (Fetter, 1994) c_s Specific heat of hyporheic sediments870 k_J k_g^{-1} K^{-1} Waples and Waples (2004)	ε_{W}	Emissivity of water	0.95	-	Dingman (2015)
Minimum and maximum water ages considered as hyporheic τ_0 , water t_0 $t_$	c_w	Specific heat of water at 10°C	4192	$\rm kJ~kg^{-1}~K^{-1}$	Kell (1972)
$ au_n$ water 1.57×10^7 $ au$ Exponent of power-law hyporheic exit-age distribution 1.39 - Poole et al. (2008) $ au$ Volumetric porosity of hyporheic zone 0.25 m^3 m^{-3} Sand and gravel, mixed (Fetter, 1994) $ au_s$ Specific heat of hyporheic sediments 870 kJ kg $^{-1}$ K $^{-1}$ Waples and Waples (2004)	$ ho_{w}$	Density of water at 10°C	999.7	${\rm kg}~{\rm m}^{-3}$	Kell (1972)
$Φ$ Volumetric porosity of hyporheic zone 0.25 $m^3 m^{-3}$ Sand and gravel, mixed (Fetter, 1994) c_s Specific heat of hyporheic sediments 870 $k_J k_g^{-1} K^{-1}$ Waples and Waples (2004)		,,	/	S	Poole et al. (2008)
c_s Specific heat of hyporheic sediments 870 $kJ kg^{-1} K^{-1}$ Waples and Waples (2004)	α	Exponent of power-law hyporheic exit-age distribution	1.39	-	Poole et al. (2008)
	Φ	Volumetric porosity of hyporheic zone	0.25	m^3m^{-3}	Sand and gravel, mixed (Fetter, 1994)
$ ho_{\rm s}$ Density of hyporheic sediments 3000 kg m ⁻³ Waples and Waples (2004)	C _S	Specific heat of hyporheic sediments	870	$kJ~kg^{-1}~K^{-1}$	Waples and Waples (2004)
	$ ho_{\mathrm{s}}$	Density of hyporheic sediments	3000	${\rm kg}~{\rm m}^{-3}$	Waples and Waples (2004)

Within the model, hyporheic water flowed into z_1 from the channel, into $z_{2..n}$ from the previous TSZ (z_{i-1}), and from every z_i back to the channel (Figure 2b). A steady-state water balance was maintained for each TSZ:

$$0 = \begin{cases} q_{\downarrow i} + q_{\uparrow i} & \text{if } i = n \\ q_{\downarrow i} - q_{\downarrow i+1} + q_{\uparrow i} & \text{otherwise,} \end{cases}$$
 (4)

where, $q_{\downarrow i}$ is water flux entering z_i (m³ s⁻¹ m⁻²), $q_{\downarrow i+1}$ is water leaving z_i and entering z_{i+1} , and $q_{\uparrow i}$ (a negative value) is water returning to the channel from z_i . By this notation, $q_{\downarrow 1}$ is total hyporheic recharge entering z_1 , which is equal to total hyporheic recharge from the channel (q_{\downarrow}). By maintaining steady state water balance for each z_i , a steady-state water balance for the entire hyporheic zone was enforced:

$$0 = q_{\downarrow} + \sum_{i=1}^{n} q_{\uparrow i}. \tag{5}$$

Thus, q_{\perp} and total q_{\uparrow} are equal in magnitude but opposite in sign.

2.2.3 | Hyporheic heat exchange model

In contrast to steady-state hyporheic water flux, simulated hyporheic heat flux was dynamic during the simulation. TempTool

allowed surface water and hyporheic water temperatures to vary in response to dynamic driving variables (Appendix B) by tracking heat storage within each TSZ, heat advection among TSZs, and the exchange of heat between hyporheic water and codiment

Instantaneous advective heat flux ($Q_{\uparrow i}$ or $Q_{\downarrow i}$) associated with any $q_{\uparrow i}$ or $q_{\downarrow i}$ at time t was dependent upon the temperature (T_i , °C) of its water source:

$$Q_{\downarrow i} = \begin{cases} q_{\downarrow i}(T_c + 273.15)c_w \rho_w, & \text{if } i = 1 \\ q_{\downarrow i}(T_{i-1} + 273.15)c_w \rho_w & \text{otherwise,} \end{cases} \tag{6}$$

and

$$Q_{\uparrow i} = q_{\uparrow i}(T_i + 273.15)c_w \rho_w, \tag{7}$$

where, c_w is the specific heat (kJ kg⁻¹ K⁻¹) and ρ_w is the density (kg m⁻³) of water and T_c is the water temperature in the channel. We calculated the instantaneous net heat exchange for each z_i as:

$$Q_i = Q_{\downarrow i} - Q_{\downarrow i+1} + Q_{\uparrow i}. \tag{8}$$

Finally, the net streambed heat flux (Q_b in Equation 1) can be expressed as the difference between heat advected into and out of the aquifer:

2.2.4 | Implementation

TempTool tracked the heat budget of the channel and hyporheic zone over time with an explicit, finite difference implementation. Heat storage in the stream channel at model time t, $H_{c.t}$ (kJ), was calculated via

$$H_{c,t} = H_{c,t-1} + Q_{c,t}A_c\Delta t, \tag{10}$$

where, $H_{c,t-1}$ (kJ) is the heat in the channel at the previous model time, $Q_{c,t}$ is the net heat flux of the channel at time (t), A_c (m²) is the wetted surface area of the stream channel, and Δt (s) is the model time step. The heat stored in z_i at a time t ($H_{i,t}$) was calculated similarly,

$$H_{i,t} = H_{i,t-1} + Q_{i,t} A_c \Delta t, \tag{11}$$

where, $H_{i,t-1}$ (kJ) is the heat in z_i at the previous model time.

TempTool calculated the temperature of channel water at model time t, $T_{\rm c.t.}$ (°C), using:

$$T_{c,t} = \frac{H_{c,t}}{V_c c_w \rho_w} - 273.15, \tag{12}$$

where, V_c (m³) is the volume of the channel.

Similarly, the temperature of TSZ z_i at time t, $T_{i,t}$ (°C), was calculated as:

$$T_{i,t} = \frac{H_{i,t}}{(V_i/\Phi)c_b\rho_b} - 273.15, \tag{13}$$

where, V_i is the water volume associated with z_i , Φ is the volumetric porosity of the hyporheic zone (m³ m⁻³), c_b (kJ kg⁻¹ K⁻¹) and ρ_b (kg m⁻³) are the specific heat and density of the saturated porous medium of the hyporheic zone. The latter two values were calculated as the porosity-weighted average of specific heat and density for water and sediment:

$$c_b = \Phi c_w + (1 - \Phi)c_s,$$
 (14)

$$\rho_b = \Phi \rho_w + (1 - \Phi)\rho_s, \tag{15}$$

where, $c_{\rm s}$ and $\rho_{\rm s}$ are the specific heat and density of the hyporheic zone sediments.

2.3 | Representative study system

Akin to investigations using experimental flumes to represent a simplified stream reach, our simulated stream did not represent a specific reach but rather a generic, archetypical stream in the inter-mountain

western U.S. Driving variables represented a semi-arid, temperate climate. We intended model scenarios with hyporheic exchange to represent expansive, coarse-grained floodplain reaches with high hyporheic exchange typified by two well-studied floodplain systems: the Nyack floodplain of the Middle Fork Flathead river (Montana, USA) (Helton et al., 2012; Whited et al., 2002) and the Umatilla river (Oregon, USA) (Arrigoni et al., 2008; Jones et al., 2008). Alluvial aquifers of floodplain reaches in the western U.S. are often vertically-constrained by bedrock below and laterally-constrained by montane valley walls. Alluvium often consists of coarse cobbles and gravels which are highly conductive (e.g., estimated hydraulic conductivity in the Umatilla river alluvial aquifer ranged between 300 and 700 m day⁻¹ [Jones et al., 2008]), thus producing expansive hyporheic zones and high gross hyporheic exchange.

2.4 | Model application

We applied TempTool using a Lagrangian reference frame, where a conceptualized 'parcel of water' is tracked as it moves downstream. Such an approach varies appropriate parameters and driving variables over time to represent the changing conditions encountered by the parcel of water as it traverses a stream course. When simulating hyporheic heat exchange, TempTool tracks the hyporheic temperature associated with various exit ages and collapses those values into an integrated mean temperature for hyporheic discharge (Equations 6–9). Therefore, the effects of variation in water temperature across the exit age distribution are integrated within the vertical dimension (i.e., at a single point). As a result, the choice of water parcel surface area is arbitrary. This approach is especially parsimonious when simulating river channels that are homogeneous in form along the stream course, as we do in this study. Under such an assumption, there is no spatial variation in geomorphic or hydrologic conditions to consider within the parcel of water.

Our simulation experiment compared seven different idealized stream channels ('scenarios'; Figure 1), each of which was subject to the same daily and seasonal atmospheric cycles (Appendix B). Within each scenario, stream channel form was uniform along the stream course. Among scenarios, stream form varied only in the size of the simulated hyporheic zone or the magnitude of riparian shade. To ease calculations, we simulated a parcel of water 1 m² in surface area. We assumed a stream depth of 0.5 m, similar to reaches of the Umatilla River and Middle Fork Flathead River from which we drew other model parameters for our simulation experiment. Simulations maintained steady-state discharge and ignored the effects of phreatic groundwater inputs in order to precisely describe the theoretical differences between shade and hyporheic exchange.

2.4.1 | Atmospheric parameters and driving variables

Windspeed and atmospheric pressure were held constant across all model scenarios at $0.01~\text{m}~\text{s}^{-1}$ and 845~mbar, respectively. These

values were the mean annual values for Pendleton, OR. See Table 1 for other atmospheric parameters held constant during simulation runs.

Time-variant inputs of air temperature (T_a), relative humidity (h_r), and atmospheric transmissivity (Γ) (Appendix B) were used in model equations describing atmospheric heat exchanges. For T_a and h_r , we used annually-repeating compound sine wave models of air temperature and relative humidity fit to data collected by weather stations adjacent to the Umatilla River floodplain, which we operated from 1 January 2003 to 31 December 2003. The Montana State University weather station (operated by Dr. Joseph A. Shaw) provided the necessary data to estimate an annually repeating sine wave of atmospheric transmissivity in the semi-arid western U.S. (Shaw, 2014). Sine wave parameters were fit using nonlinear least squares in R (R Core Team, 2021), see Appendix B for model equations and parameters.

2.4.2 | Hyporheic exchange parameterization

Cardenas (2008) argues that the exit-age distribution of at the surface water-groundwater interface scales from bedforms to bars and riverbends to basins according to a power-law. Therefore, following the methods presented in Poole et al. (2022) for our reach-scale model, we used a power-law shape (Gooseff et al., 2005; Haggerty et al., 2002):

$$f(\tau) = \tau^{-\alpha} - \tau_n^{-\alpha},\tag{16}$$

as the basis for the hyporheic exit-age density function ($E(\tau)$):

$$E(\tau) = \frac{1}{\int_{\tau_0}^{\tau_n} f(\tau') d\tau'} f(\tau), \tag{17}$$

from which the washout function, $W(\tau)$ (Butt, 1999; Coker, 2001), was derived:

$$W(\tau) = \int_{\tau}^{\tau_n} E(\tau') d\tau', \qquad (18)$$

where, α is the exponent describing the power-law shape of the exitage density function, τ is hyporheic water age (s), τ_0 and τ_n are minimum and maximum hyporheic water ages of interest (s). $E(\tau)$ describes the probability density function (PDF) representing the water age distribution of hyporheic discharge water and $W(\tau)$ describes the complementary cumulative distribution of $E(\tau)$ which provided the fraction of total q_{\perp} remaining in the hyporheic zone at τ_i .

Using $W(\tau)$, the parameters in Table 1 (i.e., τ_0 , τ_n , α), and following Poole et al. (2022), we determine q_{\downarrow}^* (s⁻¹), which is the rate of gross bidirectional hyporheic flux (q_{\downarrow} , m s⁻¹) normalized to effective aquifer thickness (S_h (m), the volume of hyporheic water per unit wetted channel area):

$$q_{\downarrow}^{*} = \frac{1}{\int_{\tau_{0}}^{\tau_{n}} W(\tau') \ d\tau'}.$$
 (19)

Thus, the rate of gross bidirectional hyporheic exchange (q_{\downarrow}) for each scenario was the product of q_{\downarrow}^* (constant across all scenarios) and S_h (which varied by scenario; Figure 1):

$$q_{\perp} = S_h q_{\perp}^*, \tag{20}$$

$$S_h = \frac{V_h \Phi}{A_c},\tag{21}$$

where, V_h is the gross combined sediment and water volume of the hyporheic zone, A_c is wetted channel area, and Φ is aquifer porosity.

We used a τ_0 value of 60 s based on a sensitivity analysis of simulated channel temperatures for various values of minimum water age ($\tau_0 \in \{10,30,60,120\}$). We determined that accounting for upwelling water with hyporheic water age of less than 60 s in the model made no appreciable difference (less than 0.01°C) to simulated channel temperatures. We used 6 months as the maximum hyporheic water age, τ_n . This value was the approximate maximum water age of hyporheic water in the Umatilla River floodplain, based on prior modelling efforts (Poole et al., 2008).

We parameterized the hyporheic model so that each z_{i+1} incorporated a range of water ages twice that of z_i , see Table 2. For example, z_1 represented a 60 s range of τ and z_2 represented a 120 s range of τ . Because the TSZs containing the youngest water contribute the largest fraction of hyporheic discharge to the channel (Figure 3; Table 2), this distribution of TSZ sizes minimized the number of TSZs necessary to provide accurate model results.

The choice of number of TSZs (n) can affect model predictions. We performed a preliminary sensitivity analysis starting with n=10 and incrementing n until resulting differences in predicted temperatures were less than 0.01°C. This threshold occurred at n=19. We therefore ran all treatment scenarios with n=18 TSZs.

Finally, per the approach outlined in Poole et al. (2022), we partitioned the total gross bidirectional hyporheic exchange among each of the hyporheic TSZ's using the washout function $W(\tau)$:

$$q_{|i} = q_i W(\tau_{i-1}),$$
 (22)

$$q_{\uparrow i} = q_{\downarrow i} - q_{\downarrow i+1}. \tag{23}$$

2.5 | Hyporheic exchange model validation

Similar to the modelled stream channel, we did not simulate any particular hyporheic zone, but instead aimed to simulate hyporheic heat exchanges typical of coarse-grained alluvial floodplains. So, to build confidence in our hyporheic model results, we performed a basic assessment of the simulated patterns of hyporheic temperature at increasing hyporheic water age across 4 days representing four different seasons of the year. We compared simulated patterns against field observations of the Nyack Floodplain, Middle Fork Flathead River, Montana, USA, from Helton et al. (2012)—a study that associated hyporheic temperatures with water age. Helton et al. (2012) published observed means (m), phases (φ) , and amplitudes (a) of the annual

TABLE 2 Fractional values of gross bidirectional exchange (q_1, q_1) and total hyporheic water storage (S_h) associated with each hyporheic TSZ assuming porosity $(\Phi) = 0.25$, power-law exponent $(\alpha) = 1.39$, $\tau_0 = 60$ s, $\tau_n = 6$ mo.

Z	$ au_{i-1}$ (s)	$ au_i$ (s)	$q_{\downarrow i}/q_{\downarrow}$ (–)	q _{↑i} / q _↑ (–)	S_i/S_h (–)
1	60	120	1.000	0.239	0.000951
2	120	240	0.761	0.183	0.00145
3	240	480	0.578	0.139	0.00220
4	480	960	0.438	0.106	0.00333
5	960	1920	0.332	0.0812	0.00503
6	1920	3840	0.251	0.0620	0.00759
7	3840	7680	0.189	0.0473	0.0114
8	7680	15 400	0.142	0.0361	0.0170
9	15 400	30 700	0.105	0.0275	0.0253
10	30 700	61 400	0.0779	0.0210	0.0372
11	61 400	123 000	0.0569	0.0160	0.0538
12	123 000	246 000	0.0409	0.0122	0.0764
13	246 000	491 000	0.0287	0.00929	0.105
14	491 000	983 000	0.0194	0.00703	0.0138
15	983 000	1 970 000	0.0123	0.00525	0.168
16	1 970 000	3 930 000	0.00708	0.00377	0.176
17	3 930 000	7 860 000	0.00331	0.00241	0.134
18	7 860 000	15 700 000	0.000899	0.000899	0.0372

temperature cycles at different hyporheic water ages and not the full temperature signals. Using these parameters, we created annual sine waves of temperature (T_{helton}) observed at different water ages in the Nyack floodplain using:

$$T_{helton} = a \sin(2\pi f \tau + \varphi) + m, \tag{24}$$

where, a is the annual amplitude (°C), f is the frequency of the wave (1/365 day⁻¹), τ is the water age (days), φ is the phase (radians), and m is the annual mean temperature (°C). Helton et al. (2012) provided the annual temperature range and the local phase (φ_l), defined as the day of the year of the maximum temperature. We divided the provided ranges by 2 to get a, and calculated the phase, in radians, using:

$$\varphi = \frac{\pi}{180}(\varphi_l - 365/4). \tag{25}$$

Because our model used atmospheric drivers from the Umatilla River, Oregon, while field observations were from the Middle Fork Flathead River, Montana, predicted and observed channel water temperatures (i.e., the temperature at hyporheic water age 0) differed markedly. Yet patterns of hyporheic temperature deviation with water age and relative to channel temperature should be similar (Luce et al., 2013) because the hydrologic and thermal properties of the Umatilla River and Nyack Floodplain aquifers are similar. Therefore, when plotting simulated hyporheic water temperature and field observations against water age, we shifted (but did not re-

scale) the y-axes to visualize patterns of hyporheic temperature deviation with water age, *relative* to channel temperature.

2.6 | Simulation experiment

2.6.1 | Treatment scenarios

For shade treatment scenarios, we altered the shaded proportion of the channel surface (s) from s=0.3 for low shade, s=0.6 for moderate shade and s=0.9 for our highest riparian shade scenario (Figure 1). By increasing shade, incoming solar radiation was reduced in proportion to s (Equation 2), but the downward longwave energy flux into the stream increased according to Equation (3). The high shade scenario (s=0.9) approximated complete canopy cover over a stream (Moore et al., 2005).

For hyporheic exchange (HE) treatments (Figure 1), we estimated the effective hyporheic zone thickness (S_h , Equation 21) for the Umatilla River floodplain, wherein the hyporheic zone extends throughout the alluvial aquifer (Jones et al., 2008). S_h (8.99 m) was determined as the product of Umatilla River floodplain width (from aerial photography), aquifer thickness (from montitoring wells, Jones et al., 2008), and aquifer porosity (Table 2) divided by baseflow wetted channel width (from aerial photography). In other systems, where the hyporheic zone occupies a fraction of the alluvial aquifer, another method of calculating S_h would be required. We used 33.33% (2.99 m), 66.66% (5.99 m), and 100% (8.99 m) of the Umatilla River S_h for our

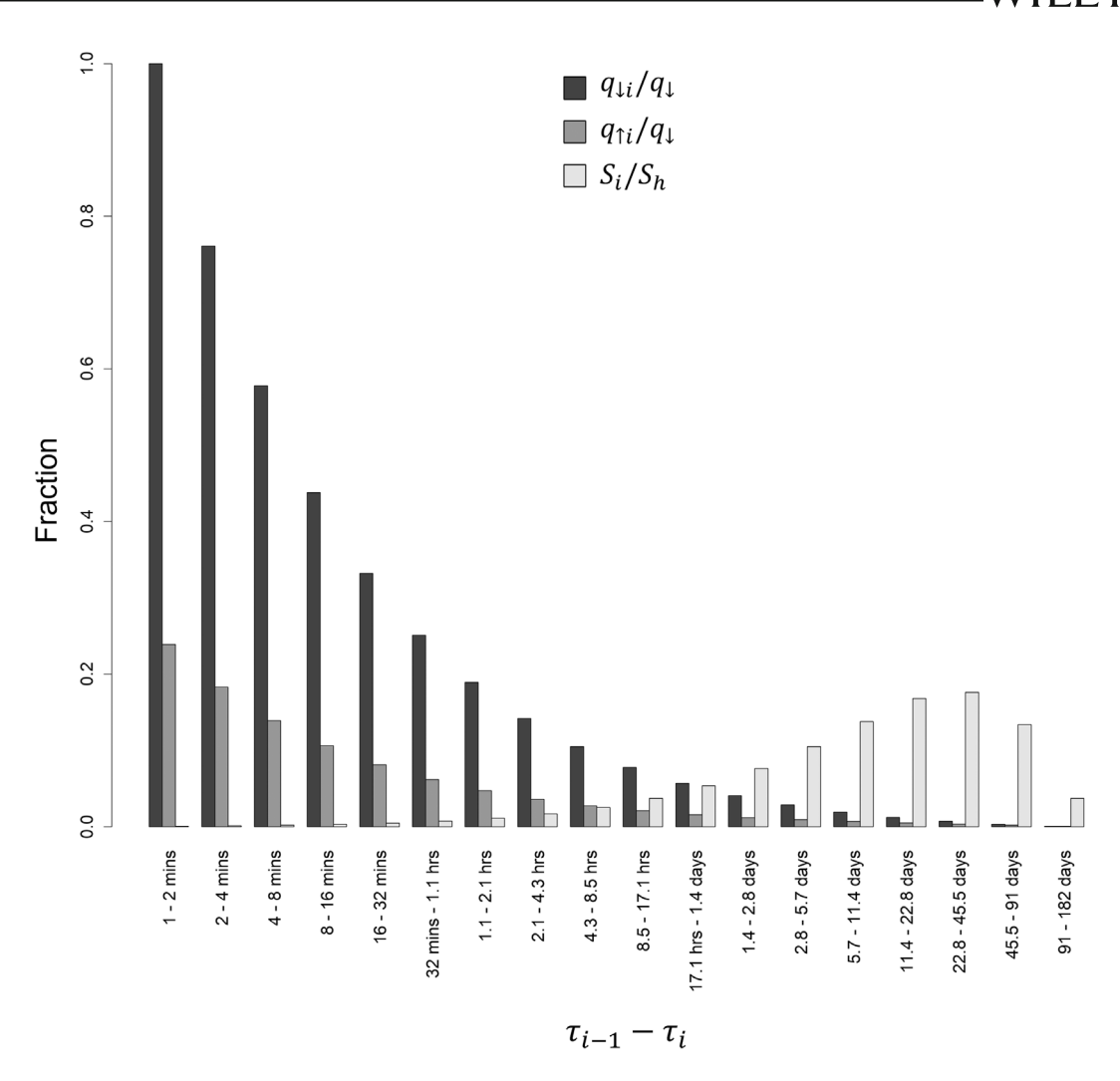


FIGURE 3 Fractional downwelling $(q_{|i}/q_{|})$, fractional upwelling $(q_{\uparrow i}/q_{\uparrow})$, and fractional hyporheic thickness (S_i/S_h) for each TSZ, shown as the hyporheic water age the TSZ encompasses. To obtain values of $q_{|j}$ and $q_{\uparrow i}$ for each hyporheic exchange scenario we multiplied the fractional values by the exchange rate—5.51e⁻⁵ (low HE), 1.103e⁻⁴ (moderate HE), and 1.654e⁻⁴ (high HE) m³ m⁻² s⁻¹. Similarly, we obtained values of S_h by multiplying the fractional volumes of each TSZ by 2.99, 5.99, and 8.99 m. These hyporheic hydrology model parameters assumed porosity (Φ) = 0.25, power-law exponent (α) = -1.39, $\tau_0 = 60$ s, $\tau_n = 182$ days.

low, moderate, and high hyporheic exchange scenarios. Using the parameters from Table 1, Equation (19) yielded a q_{\downarrow}^* of 1.59 day⁻¹. Thus, based on the values of S_h for each HE scenarios, Equation (20) yielded rates of gross bidirectional hyporheic exchange (q_{\downarrow}) of 4.75, 9.50, and 14.26 m day⁻¹ for the low, moderate, and high HE scenarios, respectively. Table 2 and Figure 3 show how q_{\uparrow} , q_{\downarrow} , and S_h are distributed among the 18 TSZs in the model, following the methods of Poole et al. (2022).

Our experimental control scenario (Figure 1) had no shade and no streambed heat exchange ($S_h = 0$ and therefore, $Q_b = 0$).

2.6.2 | Model spin-up

Initial temperatures for the channel reach and all TSZs were determined by a model spin-up procedure. We started the spin-up by initializing channel and all TSZ temperatures at 10.5°C, which was the approximate annual mean stream temperature found in the Umatilla

River watershed. We ran each model scenario for multiple years until the change in channel and TSZ temperatures on January 1 were less than 0.01°C between consecutive years. The resulting temperatures were used to initialize experimental model scenarios on January 1.

2.6.3 | Simulation parameters

All treatment scenarios (Figure 1) were simulated in TempTool using a 10 s time step. Channel temperature (T_c), the channel's net heat flux (Q_c) and all individual fluxes (see Equation 1) were recorded once an hour for two model-years.

2.6.4 Data analysis

After simulating all model scenarios in TempTool, we compared simulated heat budgets, patterns of heat flux, and temperature across all

10991085, 2023, 9, Downloaded from https://onlinelibrary.wiley.com/doi/10.1002/hyp.14973, Wiley Online Library on [1001/2024]. See the Terms and Conditions (https://onlinelibrary.wiley.com/terms-and-conditions) on Wiley Online Library for rules of use; OA articles are governed by the applicable Creative Commons Licenses

model scenarios. We calculated the annual heat budgets for each model scenario by summing, separately, the total heat-loss (negative values) and heat-gain (positive values) for each flux presented in Equation (1). We then calculated proportional values by dividing by the total flux, Q_c , for the year. We plotted both the raw (MJ y^{-1} m⁻²) and proportional values for each model scenario.

We plotted the temporal pattern of daily average heat fluxes across 1.5 years. Additionally, we plotted hourly data for 4 days, distributed throughout the year, to understand daily heat flux patterns across the four seasons. The days we chose were January 15, which represented winter, April 15 represented spring, July 15 represented summer, and October 15 represented autumn.

We also calculated and displayed daily mean channel temperature across the year, annual range in daily mean temperature, annual mean of daily mean temperature and the timing (day of year) of annual maximum and minimum daily mean temperatures. Similar to the daily heat flux plots, we show channel temperature for all scenarios for those same 4 days across the year.

RESULTS

Hyporheic zone model validation

Figure 4 shows that, in January, temperatures simulated by Temp-Tool and observed in the Nyack hyporheic zone increased similarly with increasing water age. In July, the opposite pattern was observed in the Nyack hyporheic zone and model outputtemperatures decreased with increasing residence time. In both April and October, there is no clear trend in observed hyporheic temperatures with water age in the Nyack floodplain. Similarly, there was no trend in simulated temperatures; simulated temperatures decreased and then increased with water age in April, and increased then decreased in October.

3.2 Stream channel temperature

Channel shade treatments led to a damped seasonal temperature pattern, driven by the reduction of channel temperatures in the Spring, Summer, and Autumn months (Figure 5a,c). Daily mean channel temperatures were cooler than the control scenario from approximately February to November and similar to the control stream in the winter months (Figure 5a). Summarized by Figure 5c, increasing shade caused cooler annual maximum daily mean temperature and no change in the annual minimum daily mean temperature, thus causing cooler annual mean temperatures as shade treatment increased. Shade treatments produced a positive phase shift in the seasonal temperature pattern, as summarized by the shifting of the day of annual extrema of daily mean temperature to later in the year (Figure 5d). The annual maximum daily mean temperature occurred up to 2.5 weeks later in the year as compared to the control stream (see high shade treatment, Figure 5d).

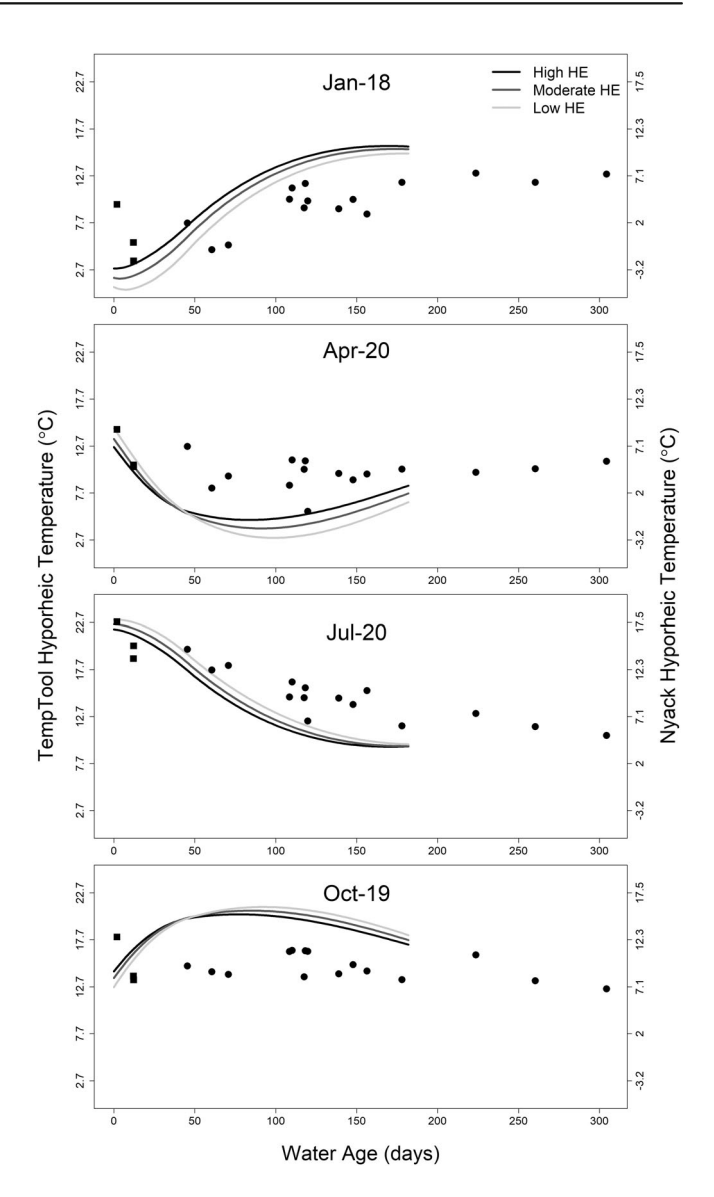


FIGURE 4 Hyporheic zone temperatures (°C) versus water age (days) at 4 days across the year. Simulated hyporheic zone temperatures of the three model scenarios are displayed by the grey lines and correspond with the left y-axis. Hyporheic zone (circles) and surface (squares) temperatures estimated using annual mean, amplitude, and phase data from Helton et al. (2012) correspond to the right v-axis. Because surface water temperatures differed between the sites, the y-axes were shifted (but not re-scaled) to compare the pattern of deviation from surface water temperature in observed versus simulated data.

Similar to channel shade scenarios, hyporheic exchange treatments also led to a damped seasonal temperature signal compared to the control reach, however this was driven by the cooling of summertime temperature and warming of winter temperatures (Figure 5b,c). HE treatments cooled daily mean stream temperatures from March through September and warmed channel temperatures from September through March. This produced a reduced annual range in temperatures but nominal change in annual mean channel temperature compared to the control stream (Figure 5c). The hyporheic

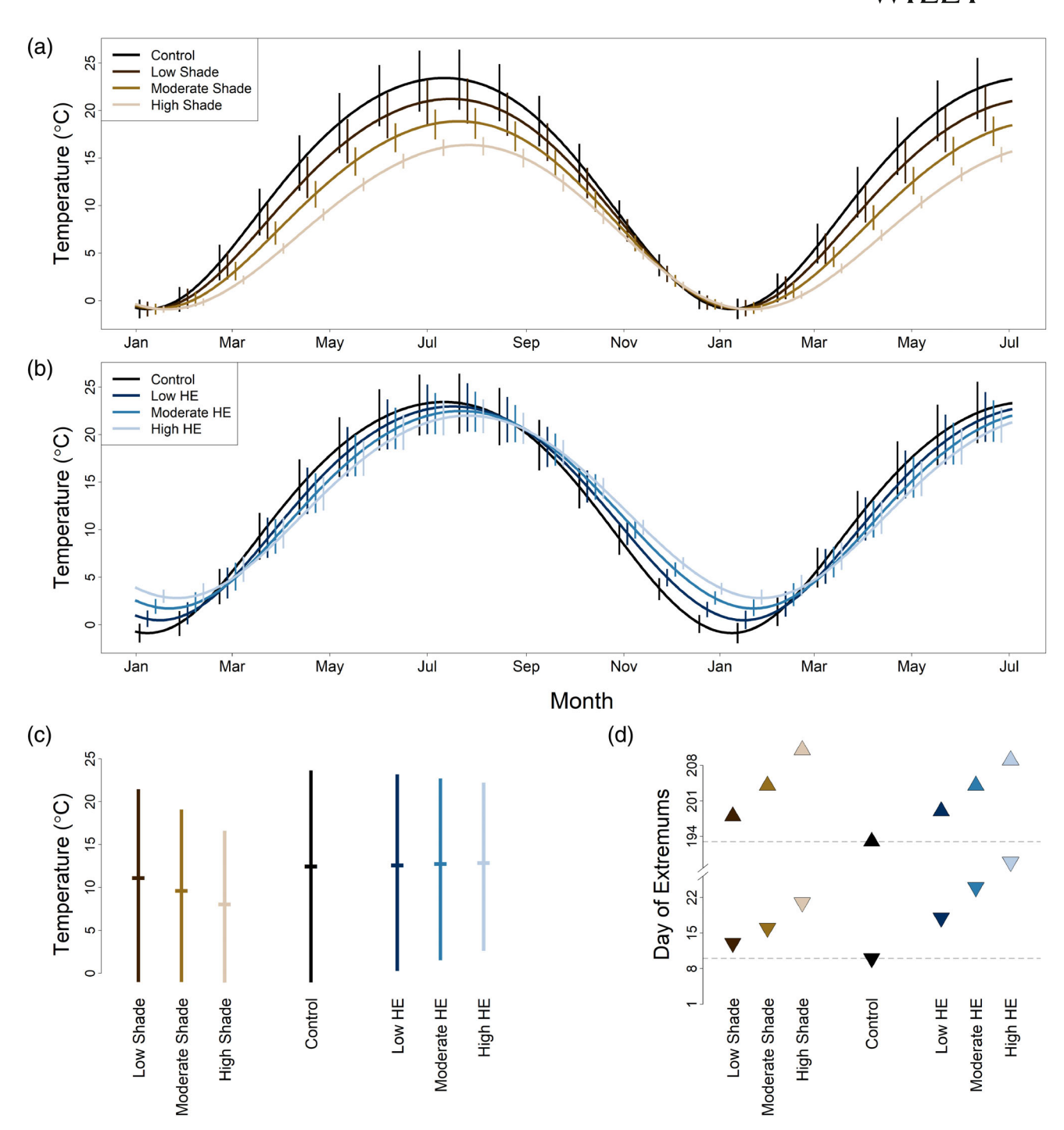


FIGURE 5 Summary of simulated seasonal cycles of daily average channel temperatures for shade (a) and HE (b) treatment scenarios. The sine-like patterns show the seasonal variation in daily average temperature and vertical lines depict diel temperature ranges every 25 days (offset by 1 week among treatment levels to avoid overplotting). Length of vertical bars in (c) shows the annual range and horizontal tick shows the annual mean of daily average temperature. The timing (day of year) of daily mean temperature extremes is shown in panel (d). Up-pointing triangles represent the days of the year the maximum daily temperature occurred for each scenario, and a down-pointing triangle represents the days of the year the minimum daily temperature occurred. Horizontal dashed lines represent the days of the year (9 and 192) when daily average temperature extrema occur for the control scenario.

exchange scenarios also produced a positive phase shift in the seasonal temperature pattern (Figure 5d), where the annual maximum daily mean temperature occurred approximately 2 weeks later in the highest HE scenario compared to the control stream.

Both shade and hyporheic exchange treatments reduced daily temperature ranges across the entire year, displayed as the lengths of vertical bars in Figure 5a,b, and shown in the daily temperature signals for the four example days in Figure 6. At the daily temperature scale,

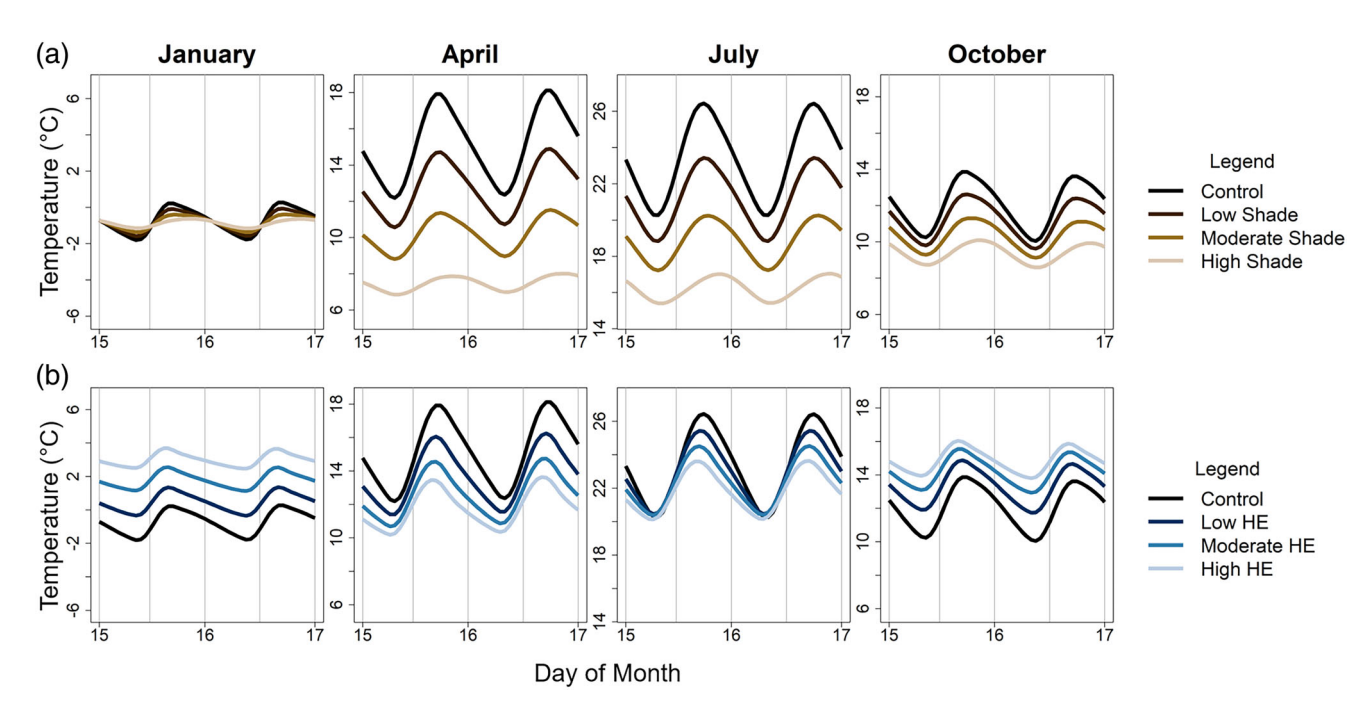


FIGURE 6 Simulated diel channel temperatures for the control, shade, and hyporheic exchange model scenarios. Forty-eight-hour channel temperatures are shown for the 15th day of January, April, July, and October for the shade treatments (a) and hyporheic exchange treatments (b). The control scenario temperature appears on all graphs in black. Note the y-axis scales origin changes across months but the temperature range is consistent across all graphs.

the most pronounced difference between shade and hyporheic exchange treatments are seen on the days in January and October, where increased hyporheic exchange caused warmer channel temperatures than the control reach whereas shade caused cooler temperatures (see October, Figure 6a) or an extreme reduction in temperature range (see January, Figure 6a). Both shade and HE produced cooler temperatures in April and July, however shade caused a much greater reduction in stream temperature than the hyporheic exchange treatments. Additionally, in April and July, shade cooled the entire daily temperature signal whereas hyporheic exchange caused the greatest cooling in the daytime, reducing the daily maximum, and modest (see April, Figure 6b) to no cooling at night (see July, Figure 6b).

3.3 | Annual heat budgets

When considering the annual heat budget of the control scenario (Figure 7a,b, middle bar) our model results showed that Q_s was the primary source of heat energy to the stream channel while Q_l and Q_e were the primary mechanisms of heat loss. Q_h was a minor component of the annual heat budget, contributing to both heat gain and heat loss of the channel, however a greater proportion of Q_h was a heat-loss mechanism in the annual heat budget of the control scenario.

Our results show that shade altered both the absolute magnitude (Figure 7b) and relative proportion (Figure 7a) of several mechanisms of atmospheric heat exchange. As channel shade increased, Q_s

contributed less in magnitude and proportion to the heat-gain budget of the stream channel. Q_{e} increased in it is *proportional* influence on the stream's annual heat budget (Figure 7a), but the absolute annual Q_{e} flux actually decreased as shade increased (Figure 7b). Additionally, the magnitude of the total annual heat flux decreased with increasing channel shade, as seen in the decreasing total widths of the annual heat flux budget bars in Figure 7b.

In contrast to shade effects, adding the additional mechanism of hyporheic exchange to the model afforded relatively small changes in magnitude to the atmospheric exchange budget (Figure 7b) although when considering the proportional budgets (Figure 7a), it appears as if the increase in Q_b causes the shown decreases in Q_s , Q_e , and Q_l . The presence of Q_b in the model increased the magnitude of total annual heat flux on the stream channel, which is directly opposite to the pattern of decreasing total annual heat flux as shade increased (Figure 7b).

3.4 | Heat flux patterns

The influence of individual heat exchanges varies across the year, where annual patterns in each heat flux are shown in Figure 8. Considering the annual patterns of the control scenario (Figure 8, row a), The range of heat gain and loss mechanisms are greatest in the summer and minimal in the winter. Q_s and Q_e show the most extreme sinusoidal seasonal patterns compared to Q_l and Q_h .

As shade increased, the amplitudes of the annual patterns in Q_s and Q_e decreased, as well as a shifting of the maximum and minimum

FOGG ET AL. WILEY 13 of 21

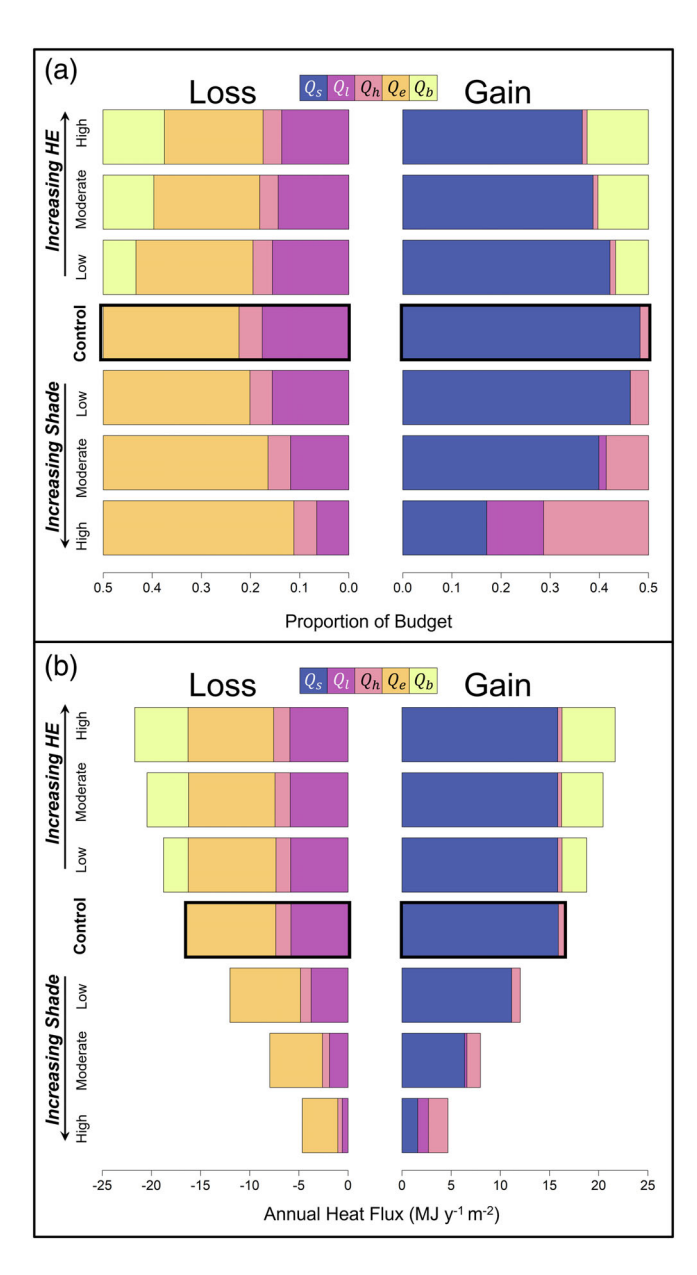


FIGURE 7 Annual heat budgets for all scenarios displayed as a proportion of the total budget (a) and the magnitude of annual heat flux (b). Heat loss mechanisms are displayed on the left and heat gain mechanisms on the right. Both (a and b) display the control scenario in the centre, outlined in bold, with hyporheic exchange and shade treatments increasing with distance from the control.

heat exchanges towards zero (Figure 8, column A), thus reducing the total annual heat exchange of these fluxes as seen in the annual heat budgets (Figure 7b). Increased shade produced minor changes in the annual patterns of Q_l and Q_h but caused positive shifts of both fluxes.

Unlike increased shade, hyporheic exchange produced minimal changes in the annual patterns of atmospheric heat fluxes (Figure 8, column B). The hyporheic exchange flux operated by counteracting the annual pattern of solar radiation, where Q_b was negative during the time of year in which Q_s peaked, that is, from approximately March to September, and Q_b was positive over the time period Q_s

was at its annual minimum, that is, from September through March of the next year.

Shade and hyporheic exchange had similar effects on the daily patterns of each individual heat flux as they did on the annual patterns (Figures 9 and 10). For all daily signals across the year, increased channel shade caused a reduction in Q_s and an increase in Q_l and reduced the total daily heat exchanges acting on the channel (see total range of all fluxes, Figure 9). As with the seasonal pattern, increasing hyporheic exchange had minimal effects on all atmospheric heat fluxes, however the opposing phase of Q_b with the phase of Q_s leads to the changes observed in the temperature signals shown in Figure 6. During the daytime, Q_b was primarily negative, removing heat from the stream channel, whereas at night, Q_b was positive, adding heat to the channel.

4 | DISCUSSION

4.1 | Hyporheic exchange model validation for heuristic application

The model we present is novel in that it represents a new combination of submodels, yet the equations of each submodel have been applied and verified in other field and laboratory study systems. We derived parameter values for atmospheric temperature exchange using data derived from experimental mesocosms (Appendix C) and built confidence in the subsurface heat transport model by comparing model results to published field results (Figure 4), and chose parameters that represent aguifer properties and rates of hyporheic exchange of an archetypal system (the Umatialla River). Although full comparisons of simulated versus observed stream channel temperatures would be useful to validate our model and demonstrate how well the model represents a particular real-world system (i.e., if our study intended to model the Umatilla River or Nyack Floodplain over a specified period of observation), there are no field sites that correspond to each scenario in our sensitivity analysis from which we can gather validation data. Instead, our approach of combining well-established and verified simulation equations with appropriate parameter values meets the objectives of our study-the development of a rigorous conceptual model that describes expected differences between thermal responses to varying levels of shade versus hyporheic exchange in a generic stream with expansive coarse-grained alluvial aquifer.

4.2 | Interactive effects of hyporheic exchange rate and water age

In TempTool, rates of q_{\downarrow} are influenced by α , which determines the shape of the power-law exit-age distribution, τ_{0} , the minimum water age of interest, and S_{h} , the effective hyporheic zone thickness. Holding α constant, higher rates of q_{\downarrow} result from either reducing τ_{0} or increasing S_{h} . Paradoxically, changes in q_{\downarrow} associated with reducing τ_{0} have only modest affects on simulated stream temperatures, while

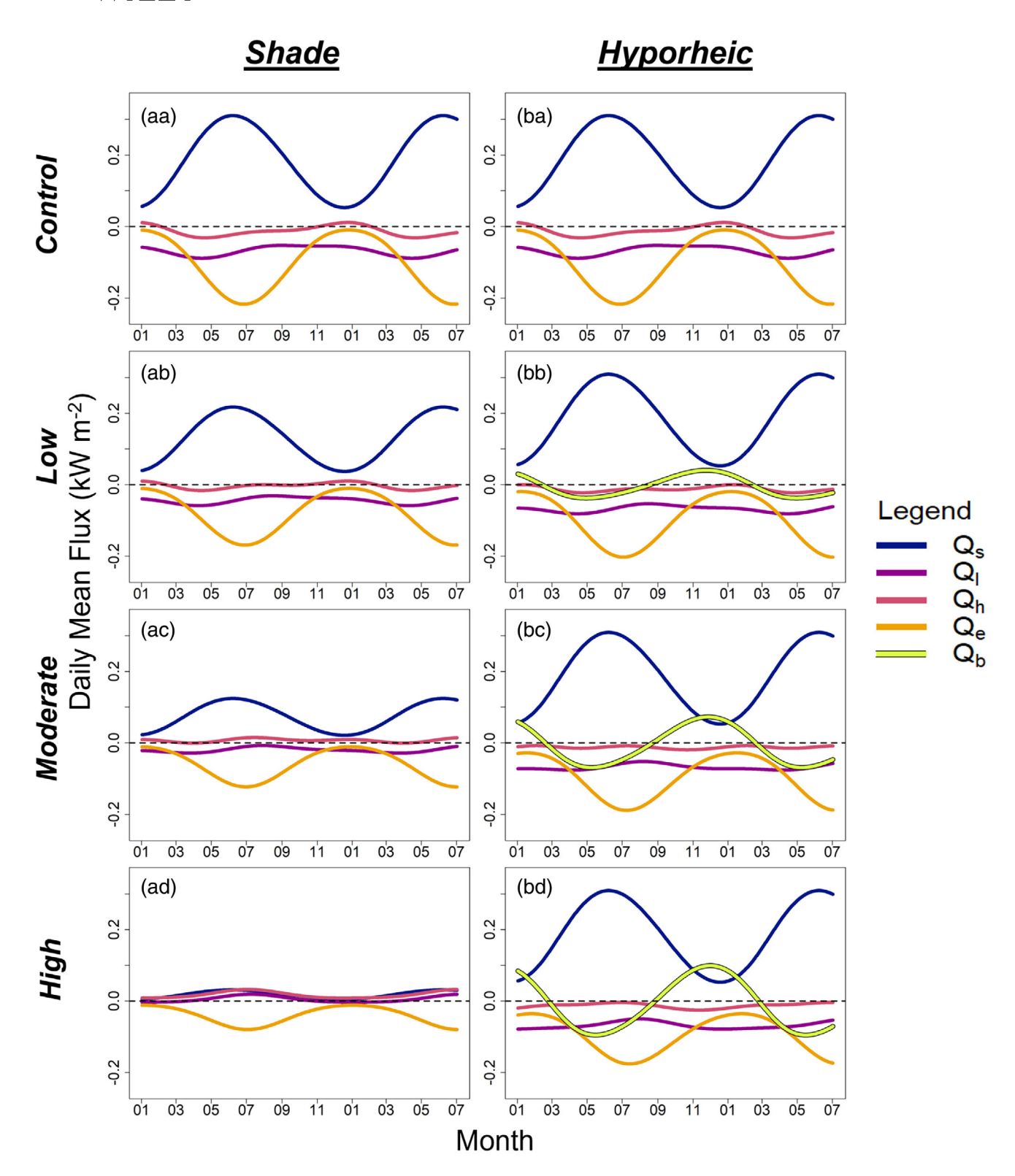


FIGURE 8 Annual patterns of daily mean heat fluxes across a year and a half for all model scenarios. The control scenario is displayed at the top (a) of both the shade treatment column (left; A) and the HE treatment column (right; B), with increasing treatment from top to bottom (b-d). The horizontal dotted line depicts zero-flux.

changes in q_{\downarrow} associated with variation in S_h yield notable effects. This paradox is resolved by understanding how reducing τ_0 versus

increasing S_h affect the exit-age distribution of the additional hyporheic exchange.

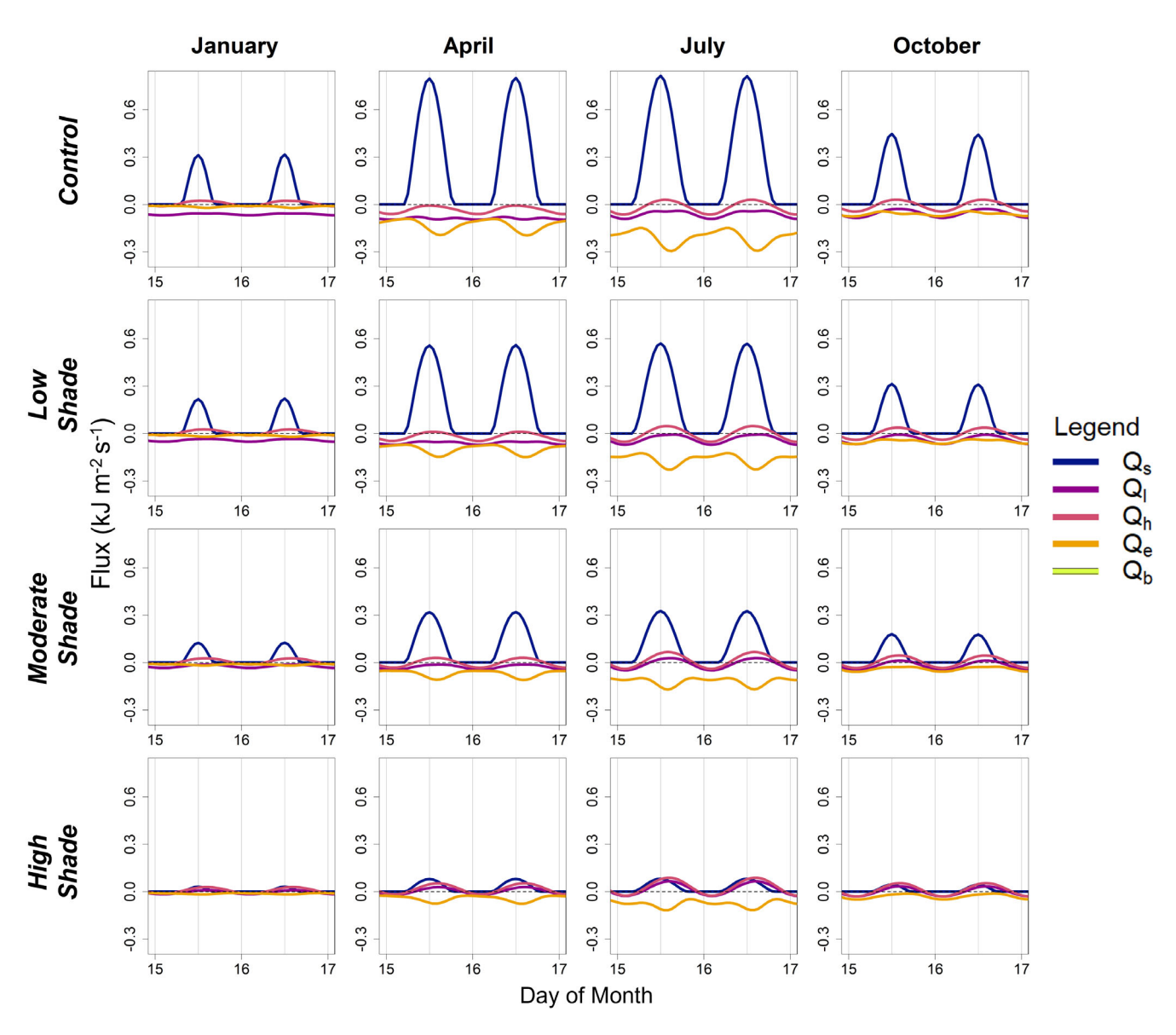


FIGURE 9 Patterns of daily heat fluxes for the control and increasing shade scenarios (row-wise). Heat fluxes are shown for a 48-h period starting on the 15th day of January, April, July, and October (column-wise).

 au_0 represents a cut-off point—water emerging from the aquifer with a water age less that au_0 will not be considered 'hyporheic exchange' by the model. The model defines water exiting the aquifer with $au< au_0$ as having never entered the hyporheic zone. Thus, conceptually, this water is treated by the model as though it remained in the channel. A reduction in au_0 causes the model to consider water with a shorter exit age as having entered the hyporheic zone. Because of the power-law shape of the exit-age distribution, a small change in au_0 can yield a large change in au_1 (Table 3). Yet because the exit age of this additional hyporheic exchange is small, the aquifer volume required to store the water as it passes through the hyporheic zone is also small, producing little associated change in hyporheic storage volume (S_h) (Table 3). This means that reducing au_0 causes a large change in calculated hyporheic exchange rate (a_1) but a small change in the thermal capacitance of the hyporheic zone. As such, the additional hyporheic

exchange considered by the model passes through a portion of the aquifer that is nearly in equilibrium with stream temperature, yielding little effect thereupon.

In contrast, changing S_h yields a proportional increase in q_{\downarrow} that is distributed proportionally to the exchange rate across all water ages from τ_0 to τ_n . Because S_h is proportional to the size of the hyporheic zone, the thermal capacitance of the system also increases in proportion to S_h . By increasing the rate of exchange through portions of the aquifer that are in thermal disequilibrium with the stream channel, the buffering effects of hyporheic exchange on channel water temperature are augmented with increasing S_h .

The difference between the temperature influence of changes in q_{\downarrow} associated with τ_0 versus S_h underscore how hyporheic heat exchange with the channel (Q_b) is a function of both the water exchange rate *and* the thermal capacitance of hyporheic sediments.

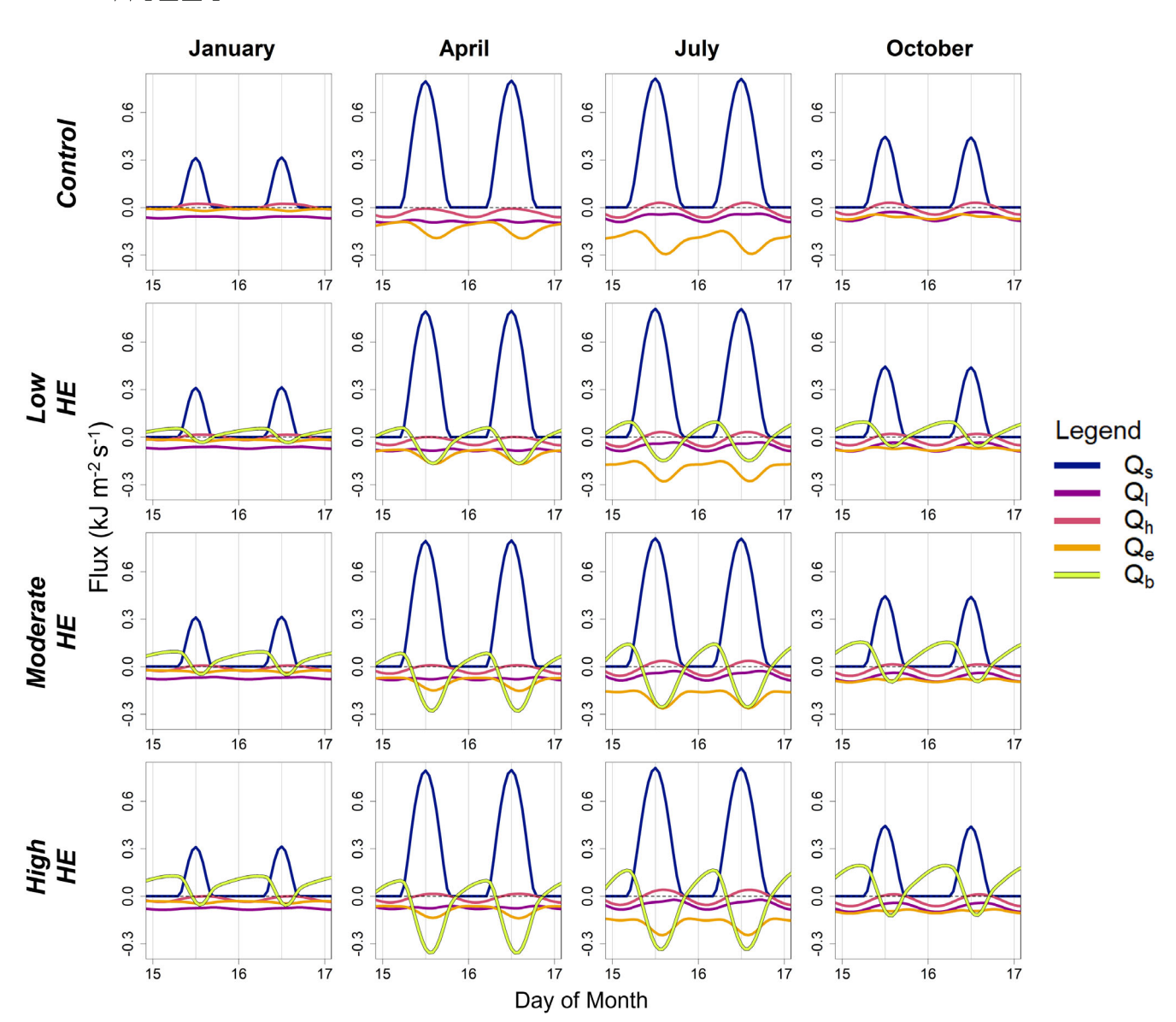


FIGURE 10 Patterns of daily heat fluxes for the control and increasing hyporheic exchange (HE) scenarios (row-wise). Heat fluxes are shown for a 48-h period starting on the 15th day of January, April, July, and October (column-wise).

TABLE 3 Calculated increases in bidirectional hyporheic exchange (q_{\downarrow}) and total hyporheic water volume (S_h) as τ_0 decreases from 120 s.

$ au_0$ (s)	q ↓ (%)	S _h (%)
120	100.0	100.0
60	131.5	100.1
30	172.7	100.2
10	265.9	100.2

Note: For all cases, $\alpha = 1.39$.

Large volumes of channel water entering, passing through, and exiting from portions of the hyporheic zone that are nearly in thermal equilibrium with the stream can have little effect on stream channel temperature. Whereas, modest volumes of channel water entering, passing

through, and exiting from portions of the hyporheic zone that are in thermal disequilibrium with the stream can have considerable effects on stream temperature. Therefore, the assumption that gross bidirectional hyporheic exchange rate alone as a surrogate for hyporheic influence on stream channel temperature is based on an overly simplistic conceptual model.

The inter-relation between water exchange rate (q_{\downarrow}) , exit age (τ) , and heat exchange (Q_b) , helps to explain a potentially confusing discrepancy between observed rates of streambed seepage from field studies (typically <2 m day⁻¹; Briggs et al., 2012; Kennedy et al., 2009; Lautz, 2012; Schneidewind et al., 2016) versus the markedly higher simulated rates of gross bidirectional hyporheic exchange (q_{\downarrow}) in our three HE scenarios (4.75, 9.50, and 14.26 m day⁻¹). Given the high values for q_{\downarrow} relative to seepage rates, one might reasonably, yet incorrectly, conclude that the simulated representation of

FOGG ET AL. WILEY 17 of 21

hyporheic exchange (and associated influence on stream temperature) must be overstated in our modelling experiment.

The differences between simulated q_{\parallel} and observed seepage rates can be attributed to our choice of τ_0 . A larger minimum water age, τ_0 , would have yielded estimates of q_1 that are in line with observed values of seepage rates. Does this mean our choice of τ_0 was 'wrong' or 'inappropriate?' Not necessarily. Seepage estimates are measured at a given spatial scale with an associated time-scale of hyporheic exit age. Yet in the model, the sensitivity of q_1 to the choice of τ_0 reflects the real-world, time-scale dependent nature of rates of gross hyporheic exchange (Poole et al., 2022). To wit, if seepage estimates could be made in such a way that they incorporated finer and finer time-scales of hyporheic exchange, observed rates of exchange in the field would also increase, even in the absence of any change in the underlying hyporheic hydrology of the system of observation. Further, as discussed above, increasing τ_0 will impart only a modest change in the predicted effects of hyporheic exchange on stream temperature. The appropriate value of τ_0 , then, should not be derived by 'tuning' the model to match field estimates of exchange rates (which have an inherent timescale). Rather, estimates of τ_0 should be derived from an understanding of the time-scales of hyporheic exchange relevant to the question at hand. In this case, hyporheic water with an exit age of 60 s or less is likely to be in thermal equilibrium with the stream. Therefore, $\tau_0 = 60$ is an appropriate value for our purpose; water with a smaller exit age will have little influence on stream channel temperature.

4.3 | Mechanisms of shade influence on surface water temperature

Our model results illustrate that the direct effects of shade on stream channel temperature operate via reducing solar radiation reaching the stream surface (Q_s) and, to a lesser degree, by impeding heat loss by longwave radiation (Q_l) from surface water. These effects can be seen in the annual heat budget (Figure 7b), where shortwave radiation dominates in the absence of shade (control scenario) but is substantially smaller than both sensible and latent heat flux in the high shade scenario. Unsurprisingly, seasonal variation in shortwave heat flux is also reduced with increasing shade (Figures 8 and 9).

Although the shift in the dominance of shortwave radiation is a direct effect of shading the stream channel, shade also influences other atmospheric fluxes, both directly and indirectly. Shade directly influences the net longwave radiation flux because riparian vegetation has a greater emissivity than air, thus increasing the bulk emissivity of the atmosphere over the stream channel as riparian vegetation increases, leading to greater downward Q_I and a reduced net loss of heat from the stream channel. The drop in peak temperatures caused by reduced solar radiation indirectly cause shade to change latent and sensible heat fluxes, even though TempTool does not directly simulate shade effects on Q_e and Q_h . Additionally, cooler peak channel temperatures further increase net Q_I , because upward Q_I is a function of channel temperature, therefore less heat was lost to the atmosphere when water temperatures are cooler.

In the field, increased riparian vegetation has the potential to influence evaporation rates by altering localized wind speed and relative humidity (Susorova et al., 2014). However, because wind speed and relative humidity drivers were the same for all model scenarios, our modelling experiment did not incorporate such effects of increased vegetation. If TempTool had incorporated reduced wind speed and increased relative humidity with increasing shade, the latent heat flux would be reduced further than seen in Figures 7 and 8. Therefore, the effects of shade on seasonal and daily temperature patterns may be modestly overstated in our model results (Figures 5 and 6) because the cooling associated with shaded latent heat exchange may be overestimated.

In total, however, increased channel shade markedly reduced the simulated seasonal and daily range of heat exchange occurring across the channel-atmosphere interface (Figures 7b and 9). This reduction in total heat exchange translates to damped stream temperature ranges at the seasonal and daily scale, as well as cooler daily mean temperatures in the Spring, Summer and Autumn and a cooler mean annual stream temperature (Figures 5 and 6a).

4.4 | Mechanisms of hyporheic influence on surface water temperature

In contrast to the effects of shade on atmospheric heat exchange mechanisms, hyporheic exchange does not directly influence atmospheric heat exchange, but rather, introduces the additional mechanism of streambed flux (Q_b) into the model. Q_b interacts with atmospheric fluxes indirectly, through the mediation of channel temperature. Therefore, increasing hyporheic exchange on a stream reach decreases the *proportional* influence of the atmospheric fluxes (Figure 7a) on the channel's heat budget, but, in fact causes minimal change in the absolute annual atmospheric heat fluxes (Figure 7b).

The pattern of storage (negative Q_b) and release (positive Q_b) of heat from the hyporheic zone is asynchronous with the pattern of Q_s at both the seasonal and daily scales (Figures 8 and 10). At the daily scale, Q_b is positive at night, adding heat to the channel when there is no incoming solar radiation. Q_b is negative during the day, removing heat from the channel while the sun adds heat. Notably, the daily pattern of Q_b does not average to zero in a 24 h period, instead Q_b averages to a positive flux in the winter months and a negative flux in the summer months. This pattern is overtly expressed in the seasonal pattern of daily mean Q_b (Figure 8) where Q_b is positive from approximately September through March of the next year, and negative approximately March through September. This asynchronicity in the pattern of Q_b compared to Q_s enables hyporheic exchange to indirectly counteract channel warming via Q_s , compared to the direct reduction of Q_s via channel shade.

In the temperate climate we simulated, the primary difference in the temperature effects of hyporheic exchange relative to shade occurs in the winter months, when the presence of hyporheic exchange warms channel temperatures. During this time of year, Q_s is at its annual minimum, Q_h contributes minimally to heat gain and Q_l

and Q_e remain negative, all which contribute to cooler winter stream channel temperatures. When hyporheic exchange is present, Q_b adds heat to the channel in the winter months, even potentially contributing more to heat-gain than Q_s (Figure 8Bc,Bd) which is the dominant heat-gain mechanism at all other times of year. The contribution of warm water to the stream channel from hyporheic exchange in the winter causes the winter channel temperatures of the HE treatment scenarios to be much warmer than the control, which had no hyporheic exchange.

4.5 | Conceptualizing shade and hyporheic exchange

Shade and hyporheic exchange have similar effects on stream temperature regimes during the spring and summer, but differ in autumn and winter (Figures 5 and 6). Heat budgets of the shade and HE scenarios demonstrate how the decreased amplitude of daily and annual temperature ranges are caused by different heat transfer mechanisms (Figures 7–10). As a conceptual simplification of their unique effects on stream heat budgets, we suggest that shade acts as a 'thermal insulator' and hyporheic exchange acts as a 'thermal capacitor'.

As a thermal insulator, shade reduces channel warming caused by shortwave radiation and channel cooling caused by longwave radiation (Figure 8A), thus limiting the net heat transfer between the stream and atmosphere (Figure 7b). Riparian shade has disproportionate effects on channel temperatures at different times of the year (Figures 5a and 6). In summer, when incoming solar radiation is at its peak, the cooling effects of reduced solar radiation are most pronounced. In winter, when solar radiation is minimal, shade has little effect on channel temperatures.

The hyporheic zone acts as a thermal capacitor—a storage zone which dynamically stores and releases heat causing reduced daily and seasonal temperature fluctuations in the channel. At both daily and seasonal time scales, hyporheic exchange removes heat from the channel during warm phases of the temperature cycle and adds heat to the channel during cool phases (Figures 5 and 6). Importantly, a nuanced understanding of the effects of hyporheic exchange on stream channel temperature requires a view of the channel and hyporheic zone as a single, integrated hydrologic and thermal system with reciprocal water and heat exchange that is asynchronous with atmospheric exchanges. Our modelling approach reflects this view by quantifying the heat budget for both components of the integrated system.

At any point across the year, then, hyporheic exchange may have a net cooling effect (summer), a net warming effect (winter), or have no measurable effect (winter-spring and summer-autumn transitions) on daily mean stream temperatures (Figure 5). This pattern has important implications for empirical studies of the effects of hyporheic exchange on stream channel temperatures. Specifically, empirical data may show little effect of hyporheic exchange on stream temperatures (Burkholder et al., 2008; Wright et al., 2005) in at least

three circumstances: (1) the hyporheic zone is small; (2) hydrologic exchange rates are low; or (3) data were collected at times of the year (Figure 8B) when the net heat exchange between the channel and streambed are at or near zero.

Similarly, when studying the effects of riparian shade on stream channel temperatures, empirical data taken in December would show that shade has little to no influence (Figure 5). Although this scenario is unlikely, it illustrates the importance of the time of year measurements are taken and the consideration of annual temperature patterns. Additionally, the effects of any variable on stream temperature may be over- or under-estimated when only a portion of the daily or annual temperature cycle is collected. Rigorous assessment of temperature patterns requires field observations and data analyses that incorporate temperature time series that span periodic channel temperature cycles (Armstrong et al., 2021).

Our results suggest that both increasing riparian shade or hyporheic exchange are viable options for stream temperature management. However, the use of either shade or hyporheic exchange for managing temperature merits careful consideration given the specific geomorphology and hydrology of a stream reach. Shade is an appropriate strategy where the geomorphic and hydrologic nature of the stream system allows establishment of riparian trees near the baseflow channel margin, such as small streams flowing through deciduous forests. In contrast, alluvial river channels migrate frequently, causing base-flow channels to be inset within a much wider annual scour zone. While mature riparian vegetation may provide shade at the margin of the scour zone, such rivers lack closed canopies along the baseflow channel edge, even in pristine settings. Therefore, establishing vegetative shade may not be a viable option for managing summertime temperature regimes in alluvial river systems. In these coarsegrained alluvial streams, past degradation of the hyporheic zone (e.g., via dredging and straightening channels) may be a primary source of impaired temperature regimes and restoring hyporheic heat capacitance may have the greatest potential for improving channel temperatures.

4.6 | Conclusion

In this study, we established 'thermal insulation' and 'thermal capacitance' as conceptualizations of how shade and hyporheic exchange alter stream heat budgets. These differing effects on stream heat budgets are apparent at the annual scale, where shade and hyporheic exchange have similar cooling effects in the summer but, in winter, hyporheic exchange warms stream temperatures and shade has negligible influence. Because of these differing seasonal effects, consideration of the annual temperature signal has important implications for temperature remediation and restoration efforts. Although temperature patterns between shade and hyporheic exchange may appear somewhat similar in the field, we suggest that understanding the mechanisms by which shade or hyporheic exchange alter a stream's heat budget is essential for management of stream channel temperature regimes.

10991085, 2023, 9, Downloaded from https://onlinelibrary.wiley.com/doi/10.1002/hyp.14973, Wiley Online Library on [1001/2024]. See the Terms and Conditions (https://onlinelibrary.wiley.com/terms-

and-conditions) on Wiley Online Library for rules of use; OA articles are governed by the applicable Creative Commons License

FOGG ET AL. WILEY 19 of 21

ACKNOWLEDGEMENTS

Support for this research was provided by the Confederated Tribes of the Umatilla Indian Reservation, US DOE—Bonneville Power Administration, Project #2007-252-00, with additional support from the USDA National Institute of Food and Agriculture (Hatch Project 1015745). Additionally, this material is based upon work supported in part by the National Science Foundation EPSCoR Cooperative Agreement OIA-1757351.

DATA AVAILABILITY STATEMENT

The data that support the findings of this study are available from the corresponding author upon reasonable request.

ORCID

S. Kathleen Fogg https://orcid.org/0000-0002-9164-1369 Geoffrey C. Poole https://orcid.org/0000-0002-8458-0203

REFERENCES

- Abdi, R., & Endreny, T. (2019). A river temperature model to assist managers in identifying thermal pollution causes and solutions. Water, 11(5), 1060.
- Anderson, E. (1954). Energy budget studies. In Water-loss investigations, Lake Hefner studies, technical report (pp. 71–119). U.S. Geological Survey Professional Paper 269 1.
- Armstrong, J. B., Fullerton, A. H., Jordan, C. E., Ebersole, J. L., Bellmore, J. R., Arismendi, I., Penaluna, B., & Reeves, G. H. (2021). The importance of warm habitat to the growth regime of cold-water fishes. *Nature Climate Change*, 11, 354–361.
- Arrigoni, A. S., Poole, G. C., Mertes, L. A. K., O'Daniel, S. J., Woessner, W. W., & Thomas, S. A. (2008). Buffered, lagged, or cooled? Disentangling hyporheic inuences on temperature cycles in stream channels. Water Resources Research, 44, 1–13. https://doi.org/10. 1029/2007WR006480
- Beschta, R. L. (1997). Riparian shade and stream temperature: An alternative perspective. *Rangelands*, 19(2), 25–28.
- Bobst, A. L., Payn, R. A., & Shaw, G. D. (2022). Groundwater-mediated inuences of beaver-mimicry stream restoration: A modeling analysis. *Journal of the American Water Resources Association*, 58(6), 1388– 1406. https://doi.org/10.1111/1752-1688.13044
- Boyd, M., & Kasper, B. (2003). Analytical methods for dynamic open channel heat and mass transfer: Methodology for heat source model version 7.0. Portland, OR, USA.
- Briggs, M. A., Lautz, L. K., McKenzie, J. M., Gordon, R. P., & Hare, D. K. (2012). Using high-resolution distributed temperature sensing to quantify spatial and temporal variability in vertical hyporheic flux. Water Resources Research, 48(2), 1–16. https://doi.org/10.1029/2011WR 011227
- Brutsaert, W., & Jirka, G. H. (1984). Measurements of wind effects on water-side controlled gas exchange in riverine systems. In D. Reidel (Ed.), Gas transfer at water surfaces. Springer.
- Burkholder, B. K., Grant, G., Haggerty, R., Khangaonkar, T., & Wampler, P. (2008). Inuence of hyporheic flow and geomorphology on temperature of a large, gravel-bed river, Clackamas River, Oregon, USA. *Hydrological Processes*, 22, 941–953. https://doi.org/10.1002/hyp
- Butt, J. B. (1999). Reaction kinetics and reactor design (2nd ed.). CRC Press, Inc.
- Campbell, G. S., & Norman, J. M. (1989). An introduction to environmental biophysics (2nd ed.). Springer.
- Cardenas, M. B. (2008). Surface water-groundwater interface geomorphology leads to scaling of residence times. *Geophysical Research Letters*, 35(8), 1–5. https://doi.org/10.1029/2008GL033753

- Chu, M. L., Knouft, J. H., Ghulam, A., Guzman, J. A., & Pan, Z. (2013). Impacts of urbanization on river flow frequency: A controlled experimental modeling-based evaluation approach. *Journal of Hydrology*, 495, 1–12. https://doi.org/10.1016/j.jhydrol.2013.04.051
- Coker, K. A. (2001). Residence time distributions in flow reactors. In Modeling of chemical kinetics and reactor design (pp. 663–761). Gulf Publishing Company.
- Danckwerts, P. V. (1953). Continuous flow systems. Distribution of residence times. Chemical Engineering Science, 2(1), 1–18. https://doi.org/10.1016/0009-2509(96)81810-0
- Demars, B. O. L., Manson, J. R., Ólafsson, J. S., Gíslason, G. M., Gudmundsdóttir, R., Woodward, G., Reiss, J., Pichler, D. E., Rasmussen, J. J., & Friberg, N. (2011). Temperature and the metabolic balance of streams. *Freshwater Biology*, *56*(6), 1106–1121. https://doi.org/10.1111/j.1365-2427.2010.02554.x
- DeWalle, D. R. (2008). Guidelines for riparian vegetative shade restoration based upon a theoretical shaded-stream model. *Journal of the American Water Resources Association*, 44(6), 1373–1387. https://doi.org/10.1111/j.1752-1688.2008.00230.x
- Dingman, S. L. (2015). Physical hydrology (3rd ed.). Wave land Press, Inc.
- Dugdale, S. J., Hannah, D. M., & Malcolm, I. A. (2017). River temperature modelling: A review of process-based approaches and future directions. *Earth-Science Reviews*, 175(January), 97–113. https://doi.org/10. 1016/j.earscirev.2017.10.009
- Evans, E. C., McGregor, G. R., & Petts, G. E. (1998). River energy budgets with special reference to river bed processes. *Hydrological Processes*, 12, 575–595. https://doi.org/10.1002/(SICI)1099-1085(19980330)12
- Faulkner, B. R., Brooks, J. R., Keenan, D. M., & Forshay, K. J. (2020). Temperature decrease along hyporheic pathlines in a large river riparian zone. *Ecohydrology*, 13(1), e2160. https://doi.org/10.1002/eco.2160
- Fetter, C. W. (1994). In R. A. McConnin (Ed.), *Applied hydrogeology* (3rd ed., p. 86). Prentice-Hall, Inc.
- Ficke, A. D., Myrick, C. A., & Hansen, L. J. (2007). Potential impacts of global climate change on freshwater fisheries. *Reviews in Fish Biology* and Fisheries, 17(4), 581-613. https://doi.org/10.1007/s11160-007-9059-5
- Follstad Shah, J. J., Dahm, C. N., Gloss, S. P., & Bernhardt, E. S. (2007). River and riparian restoration in the south west: Results of the National River Restoration Science Synthesis project. *Restoration Ecology*, 15(3), 550–562. https://doi.org/10.1111/j.1526-100X.2007. 00250.x
- Glose, A. M., Lautz, L. K., & Baker, E. A. (2017). Stream heat budget modeling with HFLUX: Model development, evaluation, and applicationsacross contrasting sites and seasons. *Environmental Modelling and Software*, 92, 213–228. https://doi.org/10.1016/j.envsoft.2017.02.021
- Gooseff, M. N., LaNier, J., Haggerty, R., & Kokkeler, K. (2005). Determining in-channel (dead zone) transient storage by comparing solute transport in a bedrock channel-alluvial channel sequence, Oregon. Water Resources Research, 41(6), 1–7. https://doi.org/10.1029/2004WR003513
- Haase, P., Pilotto, F., Li, F., Sundermann, A., Lorenz, A. W., Tonkin, J. D., & Stoll, S. (2019). Moderate warming over the past 25 years has already reorganized stream invertebrate communities. *Science of the Total Environment*, 658, 1531–1538. https://doi.org/10.1016/j.scitotenv. 2018.12.234
- Haggerty, R., Wondzell, S. M., & Johnson, M. A. (2002). Power-law residence time distribution in the hyporheic zone of a 2nd-order mountain stream. Geophysical Research Letters, 29(13), 1–4. https://doi.org/10.1029/2002GL014743
- Harvey, R., Lye, L., Khan, A., & Paterson, R. (2011). The inuence of air temperature on water temperature and the concentration of dissolved oxygen in Newfoundland Rivers. *Canadian Water Resources Journal*, 36(2), 171–192. https://doi.org/10.4296/cwrj3602849
- Hauer, F. R., Locke, H., Dreitz, V. J., Hebblewhite, M., Lowe, W. H., Muhlfeld, C. C., Nelson, C. R., Proctor, M. F., & Rood, S. B. (2016).

- Gravel-bed river floodplains are the ecological nexus of glaciated mountain landscapes. *Science Advances*, *2*(6), e1600026. https://doi.org/10.1126/sciadv.1600026
- Helton, A. M., Poole, G. C., Payn, R. A., Izurieta, C., & Stanford, J. A. (2012). Scaling flow path processes to fluvial landscapes: An integrated field and model assessment of temperature and dissolved oxygen dynamics in a river-oodplain-aquifer system. *Journal of Geophysical Research G: Biogeosciences*, 117(4), 1–13. https://doi.org/10.1029/2012JG002025
- Hester, E. T., & Doyle, M. W. (2011). Human impacts to river temperature and their effects on biological processes: A quantitative synthesis. *Journal of the American Water Resources Association*, 47(3), 571–587. https://doi.org/10.1111/j.1752-1688.2011.00525.x
- Hester, E. T., & Gooseff, M. N. (2010). Moving beyond the banks: Hyporheic restoration is fundamental to restoring ecological services and functions of streams. *Environmental Science & Technology*, 44(5), 1521–1525. https://doi.org/10.1021/es902988n
- Igbal, M. (1983). An introduction to solar radiation.
- Jankowski, K., Schindler, D. E., & Lisi, P. J. (2014). Temperature sensitivity of community respiration rates in streams is associated with watershed geomorphic features. *Ecology*, 95(10), 2707–2714.
- Jones, K. L., Poole, G. C., Woessner, W. W., Vitale, M. V., Boer, B. R., O'Daniel, S. J., Thomas, S. A., & Geffen, B. A. (2008). Geomorphology, hydrology, and aquatic vegetation drive seasonal hyporheic flow patterns across a gravel-dominated floodplain. *Hydrological Processes*, 22, 2105–2113. https://doi.org/10.1002/hyp.6810
- Justice, C., White, S. M., McCullough, D. A., Graves, D. S., & Blanchard, M. R. (2017). Can stream and riparian restoration offset climate change impacts to salmon populations? *Journal of Environmental Management*, 188, 212–227. https://doi.org/10.1016/j.jenvman.2016. 12.005
- Katz, S. L., Barnas, K., Hicks, R., Cowen, J., & Jenkinson, R. (2007). Freshwater habitat restoration actions in the Pacific northwest: A decade's investment in habitat improvement. *Restoration Ecology*, 15(3), 494–505. https://doi.org/10.1111/j.1526-100X.2007.00245.x
- Kell, G. S. (1972). Thermodynamic and transport properties of fluid water. In F. Franks (Ed.), *The physics and physical chemistry of water* (Water, Vol. 1, pp. 363–404). Springer.
- Kennedy, C. D., Genereux, D. P., Corbett, D. R., & Mitasova, H. (2009). Spatial and temporal dynamics of coupled ground water and nitrogen fluxes through a streambed in an agricultural watershed. Water Resources Research, 45(9), 1–18. https://doi.org/10.1029/ 2008WR007397
- Kurylyk, B. L., MacQuarrie, K. T. B., Linnansaari, T., Cunjak, R. A., & Curry, R. A. (2015). Preserving, augmenting, and creating cold-water thermal refugia in rivers: Concepts derived from research on the Miramichi River, New Brunswick (Canada). *Ecohydrology*, 8(6), 1095–1108. https://doi.org/10.1002/eco.1566
- Lautz, L. K. (2012). Observing temporal patterns of vertical flux through streambed sediments using time-series analysis of temperature records. *Journal of Hydrology*, 464-465, 199-215. https://doi.org/10. 1016/j.jhydrol.2012.07.006
- Luce, C. H., Tonina, D., Gariglio, F., & Applebee, R. (2013). Solutions for the diurnally forced advection-diffusion equation to estimate bulk fluid velocity and diffusivity in streambeds from temperature time series. Water Resources Research, 49(1), 488–506. https://doi.org/10.1029/ 2012WR012380
- Manning, D. W. P., Rosemond, A. D., Gulis, V., Benstead, J. P., & Kominoski, J. S. (2018). Nutrients and temperature additively increase stream microbial respiration. *Global Change Biology*, 24(1), e233–e247. https://doi.org/10.1111/gcb.13906
- Marzadri, A., Tonina, D., & Bellin, A. (2013). Quantifying the importance of daily stream water temperature fluctuations on the hyporheic thermal regime: Implication for dissolved oxygen dynamics. *Journal of Hydrology*, 507, 241–248. https://doi.org/10.1016/j.jhydrol.2013.10.030

- Moore, R. D., Spittlehouse, D. L., & Story, A. (2005). Riparian microclimate and stream temperature response to forest harvesting: A review. *Journal of the American Water Resources Association*, 7(4), 813–834. https://doi.org/10.1111/j.1752-1688.2005.tb04465.x
- Mote, P. W., Parson, E. A., Hamlet, A. F., Keeton, W. S., Lettenmaier, D., Mantua, N., Miles, E. L., Peterson, D. W., Peterson, D. L., Slaughter, R., & Snover, A. K. (2003). Preparing for climate change: The water, Salmon, and forests of the Pacific northwest. Climate Change, 61, 45–88.
- Mottola, G., Kristensen, T., & Anttila, K. (2020). Compromised thermal tolerance of cardiovascular capacity in upstream migrating Arctic char and brown trout Are hot summers threatening migrating salmonids? Conservation Physiology, 1–10. https://doi.org/10.1093/conphys/coaa101
- Munz, M., Oswald, S. E., & Schmidt, C. (2017). Coupled long-term simulation of reach-scale water and heat fluxes across the rivergroundwater interface for retrieving hyporheic residence times and temperature dynamics. Water Resources Research, 53(11), 8900–8924. https://doi.org/10.1002/2017WR020667
- O'Briain, R., Shephard, S., Matson, R., Gordon, P., & Kelly, F. L. (2020). The efficacy of riparian tree cover as a climate change adaptation tool is affected by hydromorphological alterations. *Hydrological Processes*, 34(11), 2433–2449. https://doi.org/10.1002/hyp.13739
- Ouellet, V., Secretan, Y., St-Hilaire, A., & Morin, J. (2014). Water temperature modelling in a controlled environment: Comparative study of heat budget equations. *Hydrological Processes*, 28(2), 279–292. https://doi.org/10.1002/hyp.9571
- Poole, G. C., Fogg, S. K., O'Daniel, S. J., Amerson, B. E., Reinhold, A. M., Carlson, S. P., Mohr, E. J., & Oakland, H. C. (2022). Hyporheic hydraulic geometry: Conceptualizing relationships among hyporheic exchange, storage, and water age. PLoS ONE, 17, 1–23. https://doi.org/10.1371/ journal.pone.0262080
- Poole, G. C., & Berman, C. H. (2001). An ecological perspective on in stream temperature: Natural heat dynamics and mechanisms of human-caused thermal degradation. *Environmental Management*, 27(6), 787–802. https://doi.org/10.1007/s002670010188
- Poole, G. C., O'Daniel, S. J., Jones, K. L., Woessner, W. W., Bernhardt, E. S., Helton, A. M., Stanford, J. A., Boer, B. R., & Beechie, T. J. (2008). Hydrologic spiralling: The role of multiple interactive flow paths in stream ecosystems. River Research and Applications, 24(7), 1018–1031.
- Pound, K. L., Larson, C. A., & Passy, S. I. (2021). Current distributions and future climate-driven changes in diatoms, insects and fish in U.S. streams. Global Ecology and Biogeography, 30(1), 63–78. https:// doi.org/10.1111/geb.13193
- R Core Team. (2021). R: A language and environment for statistical computing. R Core Team. http://www.r-project.org/
- Richter, A., & Kolmes, S. A. (2005). Maximum temperature limits for Chinook, Coho, and Chum Salmon, and Steelhead Trout in the Pacific north west. *Reviews in Fisheries Science*, 13(1), 23–49. https://doi.org/10.1080/10641260590885861
- Schneidewind, U., Berkel, M., Anibas, C., Vandersteen, G., Schmidt, C., Joris, I., Seuntjens, P., Batelaan, O., & Zwart, H. (2016). LPMLE3: A novel 1-D approach to study water flow in streambeds using heat as a tracer. Water Resources Research, 51, 6596–6610. https://doi.org/10.1002/2016WR018780.Received
- Shaw, J. A. (2014). MSU ORSL weather station. https://www.montana.edu/ orsl/weather.html
- Sobrino, J. A., Jiménez-Muñoz, J. C., & Verhoef, W. (2005). Canopy directional emissivity: Comparison between models. Remote Sensing of Environment, 99(3), 304–314. https://doi.org/10.1016/j.rse.2005.09.005
- Susorova, I., Azimi, P., & Stephens, B. (2014). The effects of climbing vegetation on the local microclimate, thermal performance, and air infiltration of four building facade orientations. *Building and Environment*, 76, 113–124. https://doi.org/10.1016/j.buildenv.2014.03.011

Waples, D. W., & Waples, J. S. (2004). A review and evaluation of specific heat capacities of rocks, minerals, and subsurface fluids. Part 1: Minerals and nonporous rocks. *Natural Resources Research*, 13(2), 97–122. https://doi.org/10.1023/B:NARR.0000032647. 41046.e7

- Webb, B. W., & Zhang, Y. (1997). Spatial and seasonal variability in the components of the river heat budget. *Hydrological Processes*, 11, 79–101.
- Whited, D., Stanford, J. A., & Kimball, J. S. (2002). Application of airborne multi spectral digital imagery to quantify riverine habitats at different base flows. *River Research and Applications*, 18(6), 583–594. https://doi.org/10.1002/rra.695
- Wright, K. K., Baxter, C. V., & Li, J. L. (2005). Restricted hyporheic exchange in an alluvial river system: Implications for theory and

management. Journal of the North American Benthological Society, 24(3), 447. https://doi.org/10.1899/0887-3593(2005)

SUPPORTING INFORMATION

Additional supporting information can be found online in the Supporting Information section at the end of this article.

How to cite this article: Fogg, S. K., Reinhold, A. M., O'Daniel, S. J., Hyman, A. A., & Poole, G. C. (2023). Thermal insulation versus capacitance: A simulation experiment comparing effects of shade and hyporheic exchange on daily and seasonal stream temperature cycles. *Hydrological Processes*, 37(9), e14973. https://doi.org/10.1002/hyp.14973